Earth, Planets and Space

FULL PAPER Open Access

Heat flow data and thermal structure in northeastern Japan

Takumi Matsumoto*, Ryuji Yamada and Satoshi Iizuka

Abstract

New heat flow data corrected for climate change over Northeastern Japan were obtained using the temperature profile of the borehole of the High Sensitivity Seismograph Network (Hi-net). The obtained spatial distribution of heat flow shows low heat flow on the forearc side, high heat flow along the Ou Backbone Range, and low heat flow in the plains on the back-arc side. However, the distribution is not clearly divided into high and low heat flow along the VF front; for example, the low heat flow extends from near the northern Kitakami Mountains on the forearc side to the Ou Backbone Range crossing the VF, while the high heat flow extends to the central Kitakami Mountains and Sendai plain on the forearc side. In addition, a crustal temperature structure model was developed that considers into account the presence of sedimentary layers, the temperature dependence of thermal conductivity, and differences in heat generation due to lithology. There is a good correlation between this temperature structure and the lower limit of the seismogenic layer, which is between 400 and 450 °C. Compared to previous studies, the crustal thermal structure calculation method assumed is a model whose estimated temperature distribution is sensitive to structural differences; however, a more accurate estimation of the temperature structure is possible if detailed structural information is available. On the other hand, it seems necessary to treat fluid behavior in more detail in areas of high heat flow. However, the estimation of crustal temperature structure, especially in regions with thick sedimentary layers, is considered an improvement over the previous study.

Keywords: Heat flow, Thermal structure, Climate change

*Correspondence: mtakumi@bosai.go.jp

National Research Institute for Earth Science and Disaster Resilience, 3-1 Tennodai, Tsukuba, Ibaraki 305-0006, Japan

Graphical Abstract

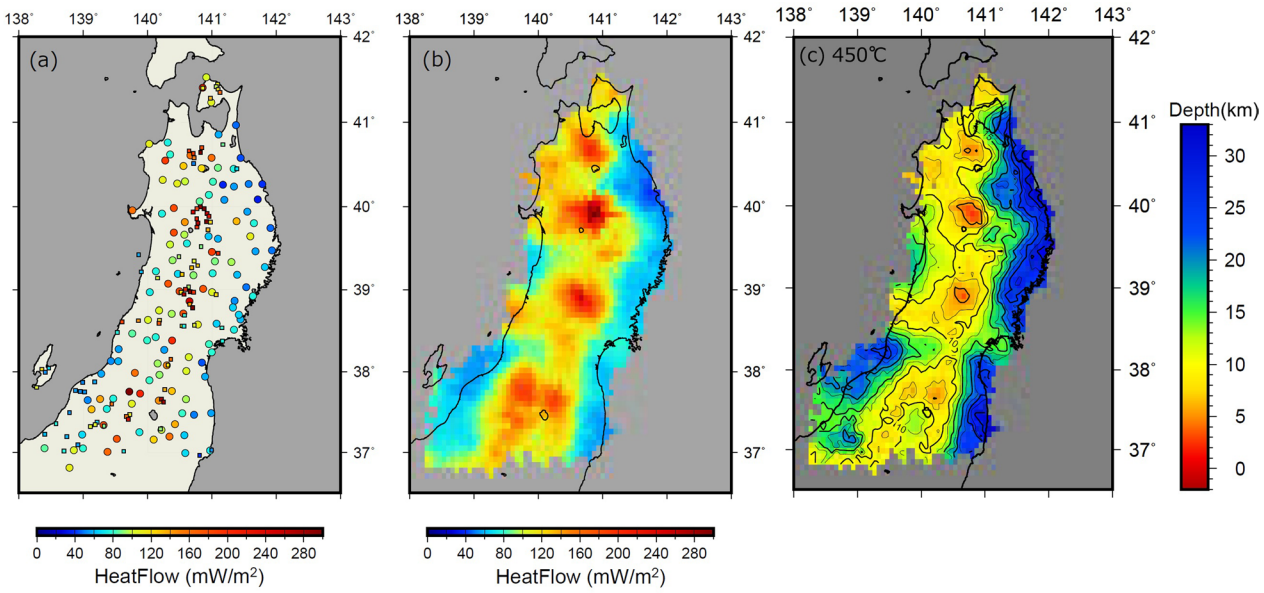

Introduction

Measurements of heat flow and estimates of subsurface temperature structure based on these measurements are essential for determining the depth of the brittle/ductile transition in the crust, which is considered to be the lower limit of the seismogenic layer of the crust (Sibson 1984), understanding trench and slow earthquakes (e.g., Yoshioka et al. 2013), understanding the recent history of plate tectonic activity (Erkan and Blackwell 2008; Tatsumi et al. 2020), and many other essential applications. A dense seismic observation network has been developed in Japan, and the detailed distribution of seismogenic layers has recently been revealed (e.g., Omuralieva et al. 2012; Yano et al. 2017).

On the other hand, heat flow data around the Japanese archipelago were first presented by Uyeda and Horai (1964), and many measurements were made in the terrestrial and oceanic regions (e.g., Yamano 1995). The distribution of available boreholes has constrained land heat flow measurement in Japan, but many data were obtained in non-geothermal areas. However, there are many areas with low data distribution density. Here we attempt to compensate for this spatial distribution by measuring new heat flow in Northeastern Japan. We investigated temperature profiles of 132 borehole wells (100–200 m depth) in the Northeastern Japan of the Hi-net, seismic network, a uniformly distributed seismic network over land in the Japanese archipelago. Thermal conductivity was measured from the deepest rock cores obtained during borehole drilling or estimated from lithology when a measurement was difficult. From the results of processing the data, taking into account the effects of climate change and other factors, a new heat flow map was created to estimate the subsurface temperature structure.

Tectonic setting

Northeastern Japan arc is one of the typical island arc–trench systems formed by the subduction of cold plates in ancient times. Northeastern Japan is in contact with the Eurasian plate on the eastern side of the Sea of Japan. To the east is the epicenter of the 2011 off the Pacific coast of Tohoku earthquake, which caused a large resonance slip of over 60 m (Ito et al. 2011), and The Pacific Plate subducts westward at the Japan Trench under the Japanese islands. There are many volcanoes and earthquakes in Northeastern Japan, and these active volcanoes, seismogenic zone, and active faults are distributed almost parallel to the Japan Trench, the boundary of the plates. Active volcanoes are mainly distributed along the Ou Backbone Range, and the eastern edge of their distribution area forms the volcanic front. The distribution of volcanoes on the back-arc side extends to the Sea of Japan side in Northeastern Japan.

The opening of the Yamato Basin on the back-arc side occurred from 21 to 15 Ma, and normal faulting developed in the extensional stress field from the present Japan Sea coast to the forearc from 15 to 13.5 Ma, when the volcanic front also moved in the trench direction (Yoshida et al. 2013). After the opening of the Japan Sea ended around 13.5 Ma, a period of neutral stress field continued (Yoshida et al. 2013). At about 4 Ma, the westward movement of the Pacific Plate increased (Pollitz 1986), followed by strong compression of the entire island arc. It is thought that most of the Miocene normal faults were reactivated, and the volcanic arc was uplifted (Yoshida et al. 2013). These imply tectonic inversion (Sato 1994) (see Fig. 1).

Data collection

Hi-net borehole temperature logging data

After the disastrous 1995 Kobe earthquake, a new national project has drastically improved Japan's seismic observation system. Many strong-motion, high-sensitivity, and broadband seismographs were installed to construct dense and uniform networks covering the whole of Japan. (Okada et al. 2004). After the 2011 off the Pacific coast of Tohoku Earthquake, a submarine observation network was also constructed, and this integrated ocean–land observation network is called MOWLAS (Aoi et al. 2020). The high-sensitivity seismic observation network consisting of about 700 stations is called Hi-net.

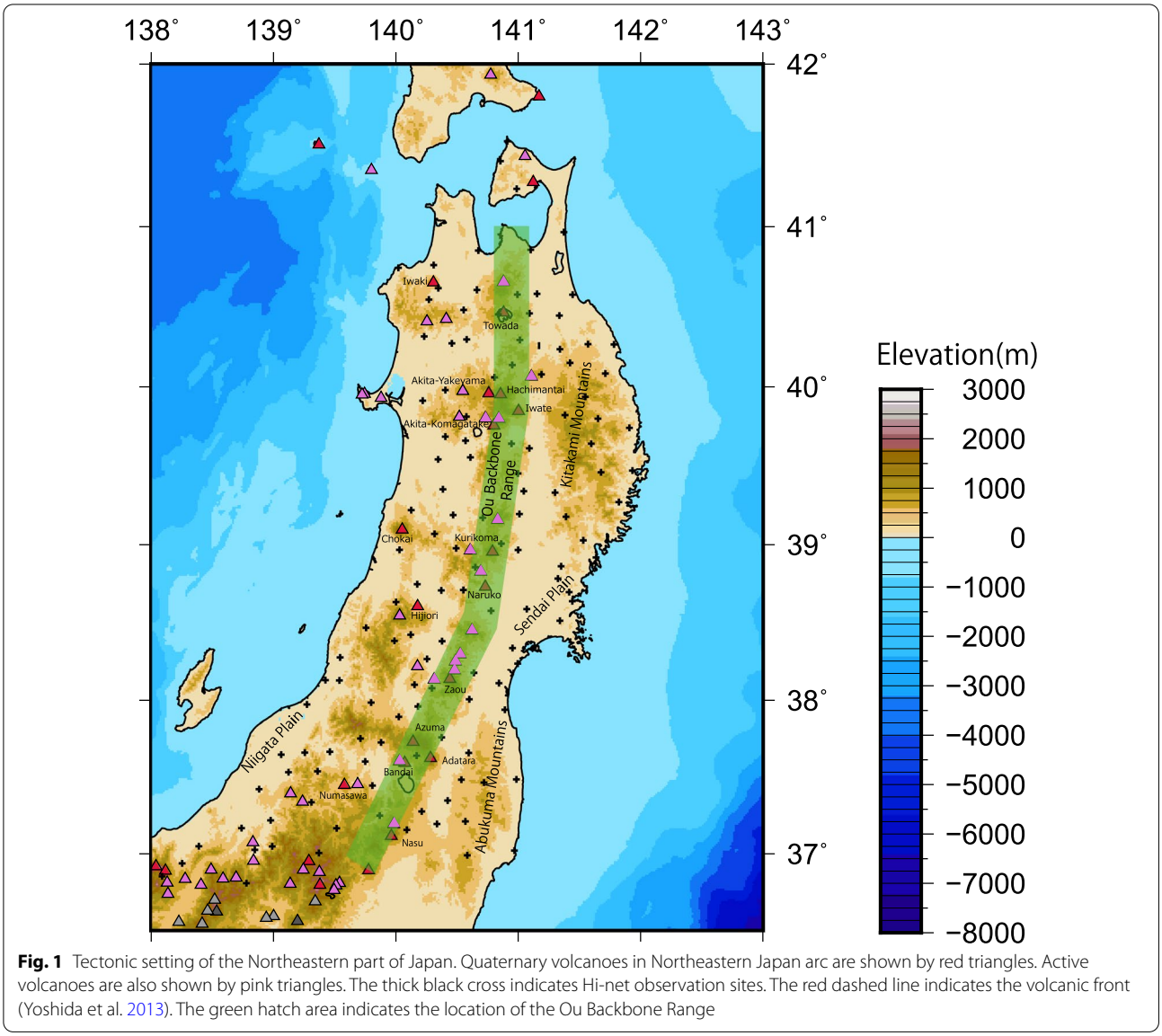

Fig. 1 Tectonic setting of the Northeastern part of Japan. Quaternary volcanoes in Northeastern Japan arc are shown by red triangles. Active volcanoes are also shown by pink triangles. The thick black cross indicates Hi-net observation sites. The red dashed line indicates the volcanic front (Yoshida et al. 2013). The green hatch area indicates the location of the Ou Backbone Range

Since the limit of the depth of the epicenter of inland earthquakes in Japan is usually 15–20 km, it was necessary to construct a seismic observation network at intervals of 15–20 km in order to accurately determine the depth of the epicenter of earthquakes of such depth. In order to perform stable and highly sensitive seismic observations by avoiding noise on the ground surface, seismometers are installed at the bottom of a borehole at a depth of more than 100 m at each Hi-net station. Although the majority of the Hi-net stations have boreholes of 100–200 m in depth, deep observation wells were made at some specific sites if necessary. Hi-net borehole wells are cased and full-hole cemented around the casing for long-term stable observation (Okada et al. 2004). Therefore, there is no ingress or egress of groundwater, and good-quality temperature profiles are expected to be obtained.

In Northeastern Japan, Hi-net stations were constructed between 1998 and 2000. In addition, two stations were constructed in 2012 to replace those damaged by the Tohoku earthquake. Of the 133 Hi-net stations in Northeastern Japan, 132 stations conducted thermal logging of each borehole well within a few months of the completion of drilling. For the observation wells with a depth of 100 m to 200 m, the effect of thermal disturbance caused by mud circulation during drilling is considered to be small because the time required for drilling is short, and the temperature difference between the surface and the bottom of the well is slight, generally within 10 °C. In order to test this hypothesis, eight observation wells were re-examined after a certain period. However, it is not easy to conduct temperature logging in Hi-net boreholes with seismometers installed.

Therefore, about six years after the drilling, the temperature logging was conducted by inserting an optical fiber into the borehole. The distributed temperature sensor (DTS) used was a Sumitomo Electric SUT-2. DTS can measure a physical quantity along the fiber length at many multiplexed points. Dakin et al. (1985) were the first to demonstrate that the temperature could be determined from measured Stokes and anti-Stokes Raman scattering ratio. The typical performance of a Raman-based DTS is 1 m spatial resolution and 1 K temperature uncertainty for a 5-min measurement integration period, with a sensing range of 10 km.

However, these figures can be substantially improved if the experimental conditions are alleviated (i.e., shorter range, worse spatial resolution) (Thévenaz 2006). For example, the performance of SUT-2 is 0.5 m spatial resolution and 0.1 K temperature uncertainty for a one-hour measurement integration period, with a sensing range of 2 km. As a result, the difference between the temperature logging data obtained a few months after the end of drilling and the data obtained a few years later was small, and the temperature profiles obtained in these two periods can now be considered to be of good quality with little influence from the temperature disturbance caused by drilling (see Fig. 2).

Thermal conductivity

Rock cores are collected from the deepest 25 m or 30 m section in a typical Hi-net borehole. However, in boreholes drilled to depths of 1,000 m or more, rock cores were collected from multiple sections at intervals of 250 to 500 m. The thermal conductivity of these rock cores was measured using a Kyoto Electronics QTM-500. The thermal conductivity measurement device used in this study, the QTM-500 Rapid Thermal Conductivity Meter, is based on the hot wire method (e.g., Arakawa and Shinohara 1981). The QTM-500 is a one-dimensional (linear) heat wire placed on the surface or inside of a sample to measure the temperature increase inside the sample when a certain amount of heat (electric power) is applied, and the thermal conductivity is calculated (e.g., Tadai et al. 2009).

Rock cores from about 50% of the Hi-net boreholes were shaped, and thermal conductivity was measured using the QTM-500. In addition, for about 50% of the Hi-net boreholes where thermal conductivity measurement by the hot wire method was difficult due to fracturing of the rock core, thermal conductivity was estimated by referring to the columnar map and PS logging results of the well. In the estimation, we referred to Sato et al (1999) and Gueguen and Palciauskas (1994) (see Table 1).

For the thermal conductivity of sedimentary formations, which are particularly difficult to core-shape, data from Hi-net 2000m-class boreholes drilled in the Kanto region were used as a reference, as described below.

Generally, the thermal conductivity of surface soils in plain areas is about 1.2 Wm^{-1} K^{-1}. However, according to the results of rock core tests in Hi-net boreholes in the Kanto region, the thermal conductivity is about 1.0–1.2 W m^{-1} K^{-1}, even in Tertiary sedimentary layers when the elastic wave velocity V_p is less than 2.0 km s^{-1} (Suzuki and Omura 1999). Since PS velocity logging was performed in all Hi-net boreholes during construction, based on the PS velocity data, the thermal conductivity was set as 1.2 W m^{-1} K^{-1} for Tertiary sedimentary layers in Northeastern Japan with elastic wave velocity V_p less than 2.0 km s^{-1} and 1.0 Wm^{-1} K^{-1} for Quaternary sedimentary layers.

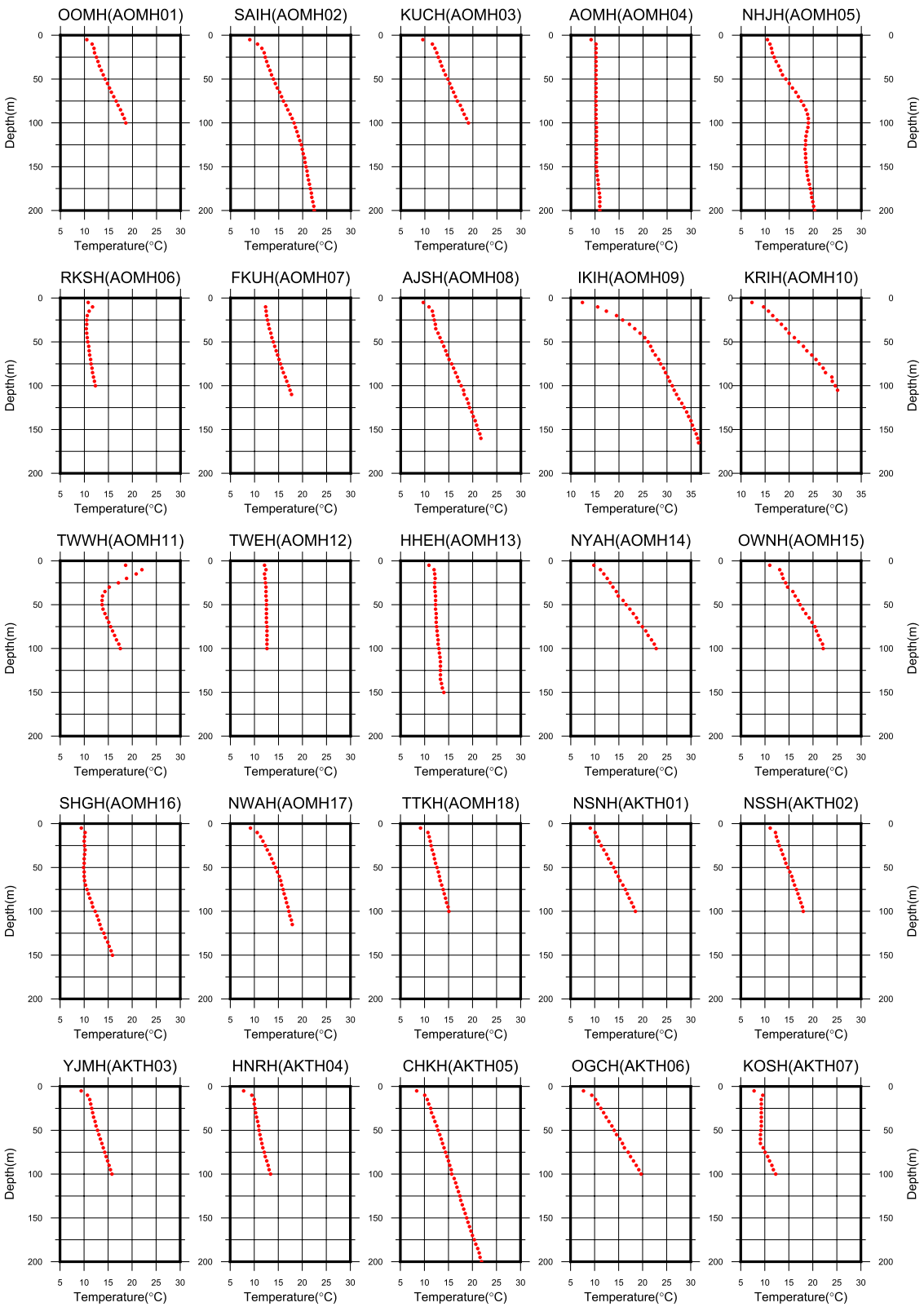

Fig. 2 Temperature profiles of Hi-net boreholes. The red dots show the data from the first temperature logging, and the blue dots show the data from the second temperature logging performed using DTS

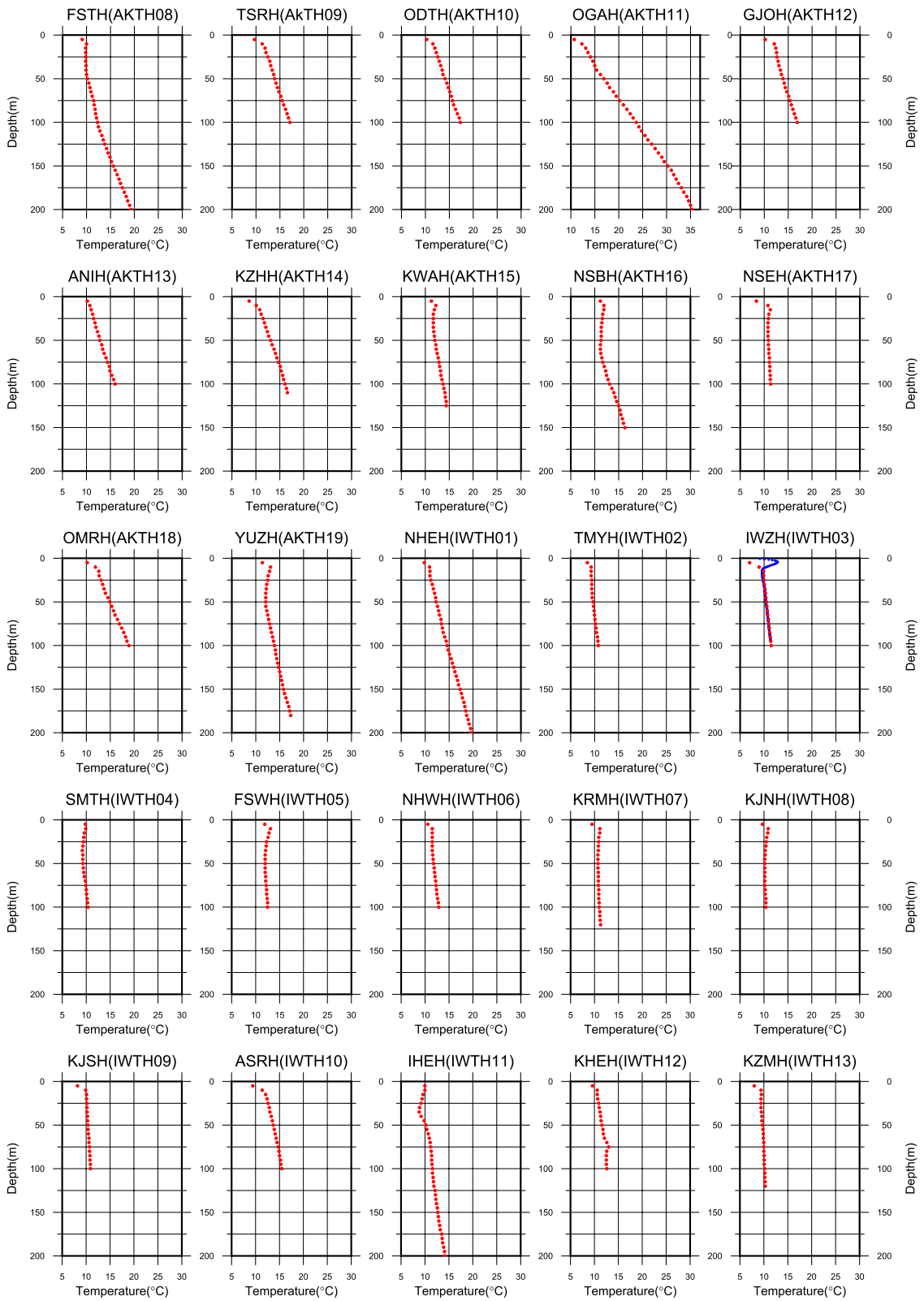

Fig. 2 continued

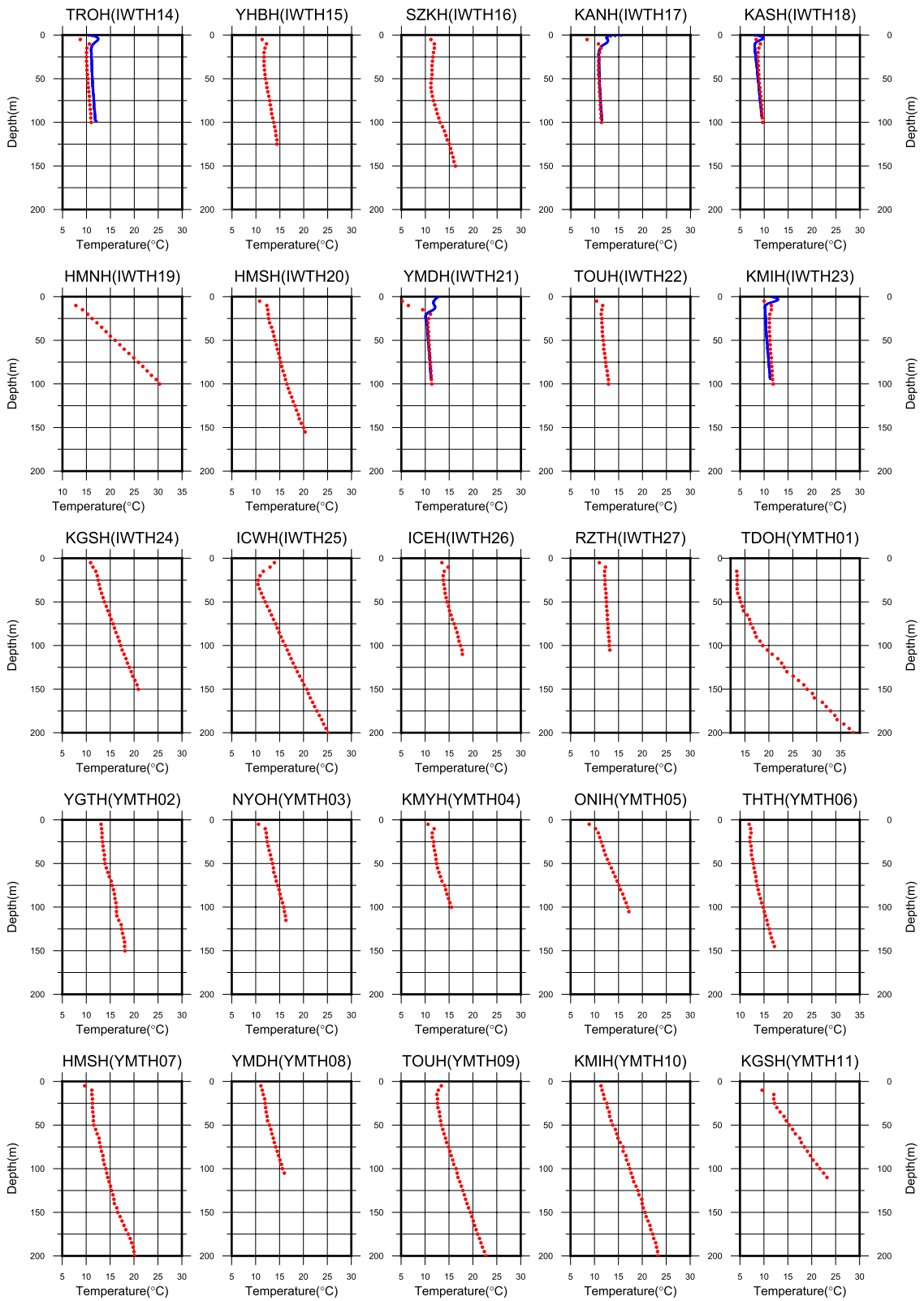

Fig. 2 continued

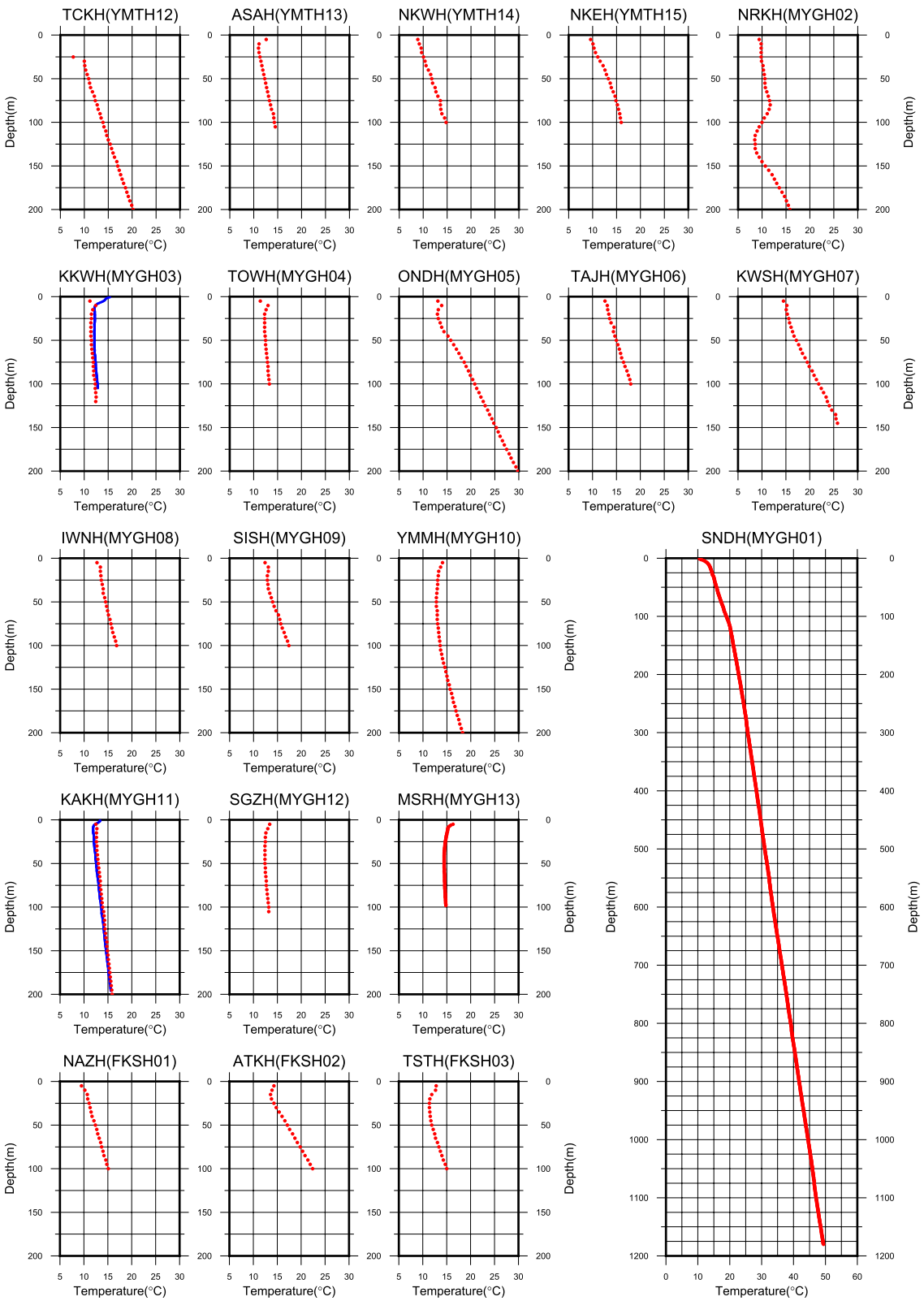

Fig. 2 continued

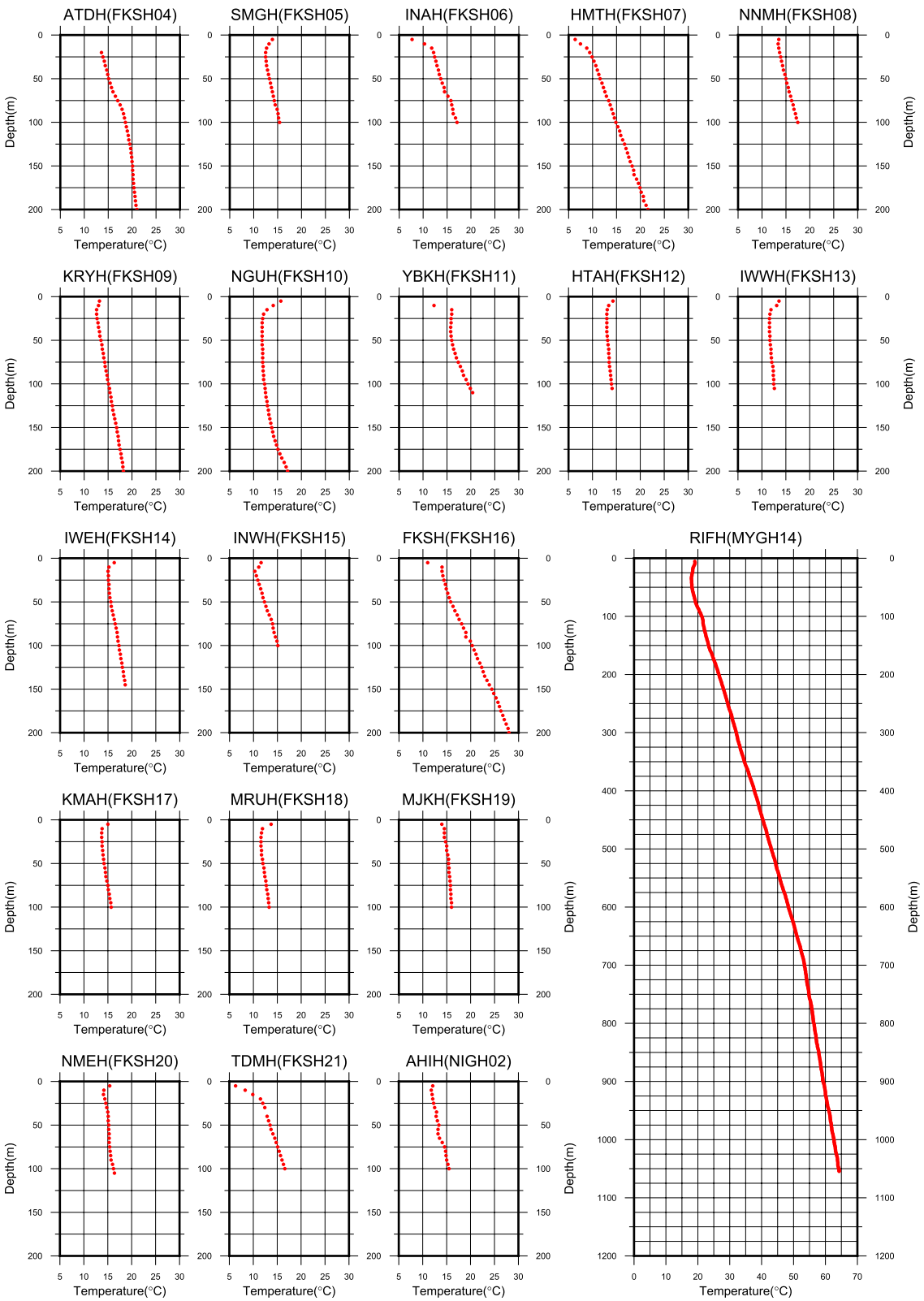

Fig. 2 continued

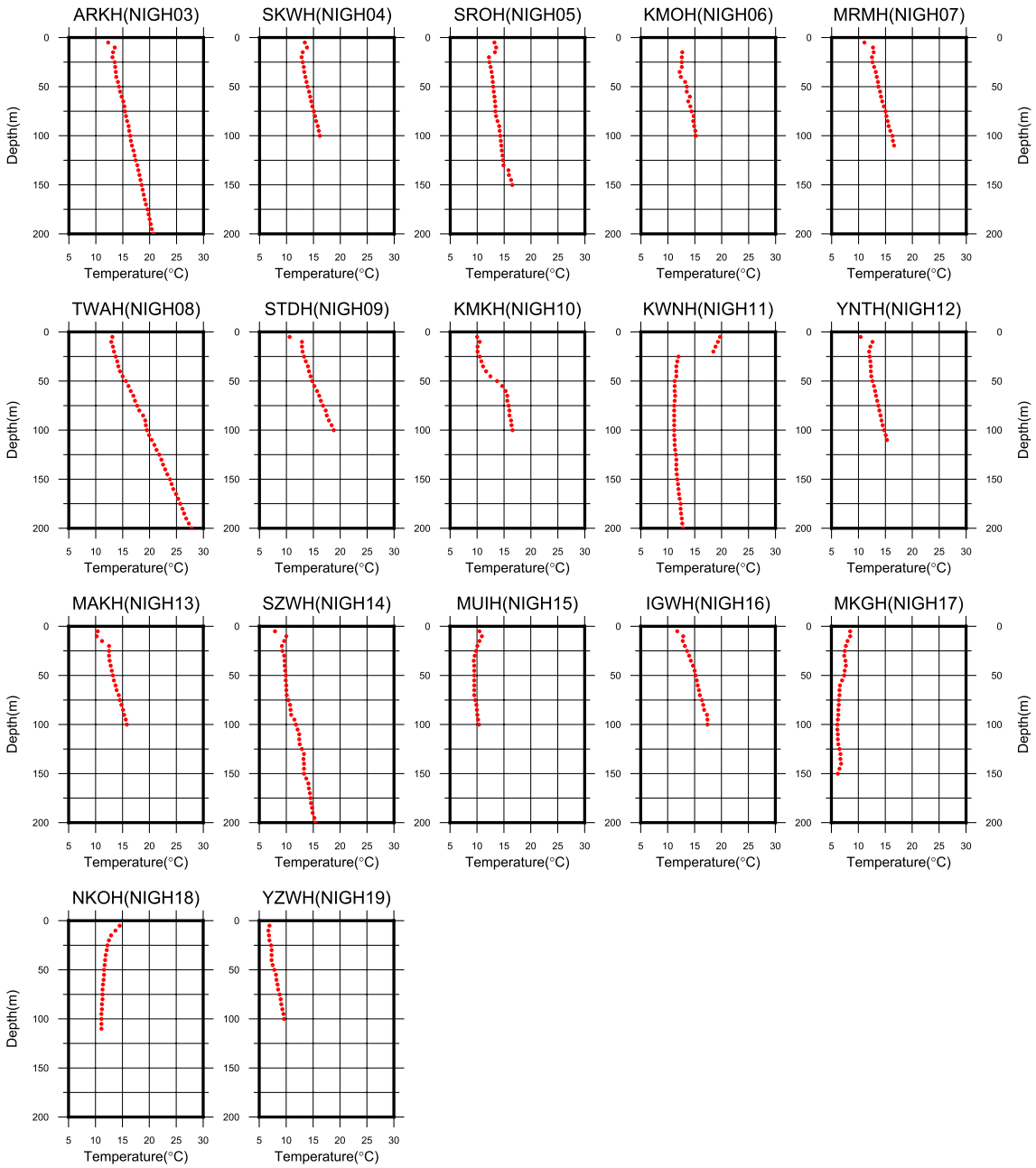

Fig. 2 continued

Terrestrial heat flow

Data quality

Borehole wells used for heat flow analysis are often deeper than 300 m to avoid thermal disturbance caused by climate change, groundwater flow, and topographic effects. In the case of the Hi-net borehole well, drilling down to the basement rock is desirable to avoid surface ground noise. However, due to the spatial arrangement of the observation points, some wells are constructed in areas with thick sedimentary layers. Furthermore, as mentioned earlier, the Hi-net borehole wells are covered with a casing, and full-hole cementing prevents water inflow into the borehole, so very stable temperature gradient data are expected to be obtained.

In this study, the quality of the temperature logging data were evaluated by the characteristics of the T–D curve, referring to Erkan (2015), who performed heat flow analysis using shallow wells. The data were classified

Table 1 Thermal conductivity and thermal diffusivity by lithology

Lithology	Thermal conductivity ($Wm^{-1} K^{-1}$)	Thermal diffusivity ($m^2 s^{-1}$)
Granite, basalt, andesite, schist	2.86	1.05×10^{-6}
Gabbro, diorite, rhyolite	2.36	8.40×10^{-7}
Sedimentary Paleogene (sandstone)	3.19	1.15×10^{-6}
Sedimentary Paleogene (tuff)	2.68	9.51×10^{-7}
Sedimentary Neogene (sandsotne)	1.56/1.2	9.63×10^{-7}
Sedimentary Neogene (tuff)	1.62/1.2	9.21×10^{-7}
Sedimentary Quaternary	1.2/1.0	5.80×10^{-7}

See Sato et al. (1999) and Gueguen and Palciauskas (1994)

into four classes; A, B, C, and D. Sections up to 10 m in depth were excluded from the evaluation because they are likely to be affected by seasonal variations in surface temperature and artificial ground improvements such as embankments and cuttings.

Temperature log data classified as Class-A are those that show the effects of long-term climate change over the past century in the range of 10 to 30 m below the surface, are largely undisturbed except for temperature inversions, and also show a heat conduction type at depths below 50 m and are undisturbed throughout the entire area. For wells deeper than 100 m, linearity must be obtained in temperature logging data at depths greater than 100 m.

The temperature log data classified as Class-B show the effects of long-term climate change over the past century in the range of 10–30 m from the surface and shows the effects of groundwater flow and other factors in addition to a temperature inversion, but without significant disturbance and also shows a heat conduction type in about 50% of the sections at depths of 50 m or deeper.

The temperature logging data classified as Class-C has poor linearity and is greatly affected by groundwater flow and other factors, but there is no significant disturbance in the deepest 25-m section. The temperature logging data likely strongly influenced by groundwater throughout the section were classified as Class-D. This Class-D data was deemed unsuitable for heat flow analysis. Examples of T–D curves for the four classes are shown in Fig. 3.

The rock cores were collected only in the deepest 25-m or 30-m section. Therefore, the temperature gradient in the deepest 20-m section where the rock core was collected was used to analyze the heat flow. The temperature gradients in the deepest 50 m or 200 m sections where the lithology remains the same were used to analyze the heat flow for the two wells over 1000 m. In determining the temperature gradient, a regression line was obtained using the least-squares method, which was used as the temperature gradient before correction.

Climate change correction

The subsurface temperature field also records climatic changes at the surface. The effects of Pleistocene glaciation over several hundred thousand years extend several thousand meters below the surface, and climate change since the end of the nineteenth century has been particularly significant, affecting depths of 50 to 100 m (Jessop 1990). Therefore, in determining the heat flow, it is

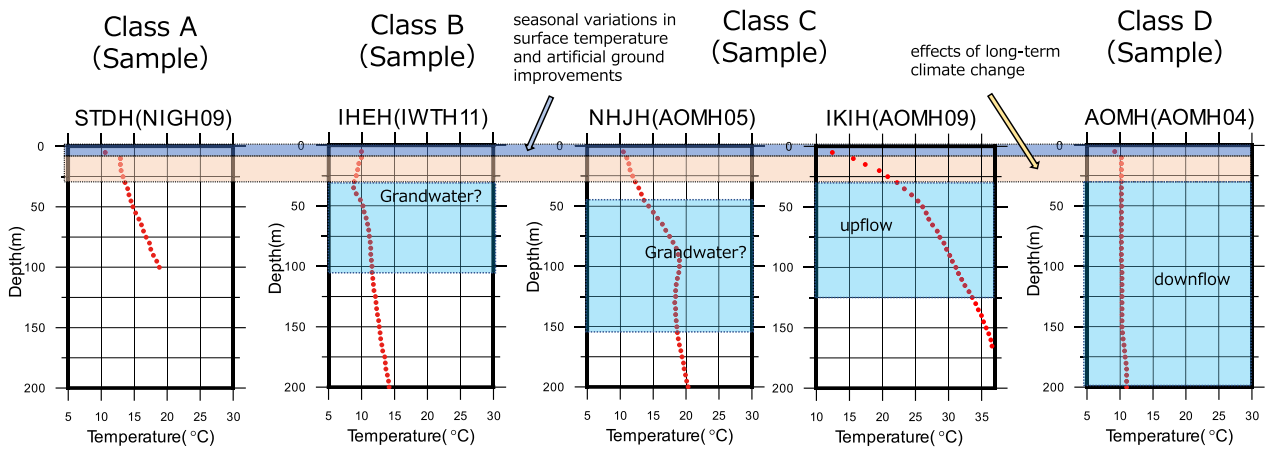

Fig. 3 Example of well temperature logging data quality. The blue section in the background (0–10 m depth) is affected by seasonal variations in surface temperature, artificial ground modification, and soil cut and fill and is excluded from the evaluation. The section in the beige background (10–30 m depth) is excluded from the evaluation because it is mainly affected by the temperature increase over the past 100 years. Sections that may be affected by groundwater are shown with a sky-blue background. Class-A data are considered high data quality, while Class-D data are considered unsuitable for heat flow analysis

necessary to correct the effects of climate change for wells with depths between 100 and 200 m in the Hi-net standard specifications.

The Japan Meteorological Agency (JMA) analyzes that the annual mean temperature in Japan has been rising with various fluctuations and is rising at a rate of 1.28 °C per 100 years in the long term (JMA 2022). However, it is said that there is a difference in the trend of temperature increase between suburban and non-urban areas, known as the heat island phenomenon. Matsumoto (2007) calculated heat flow corrected for the effects of climate change, assuming a uniform 2.0 °C temperature rise over the past 100 years in the Japanese archipelago and considering the temperature rise in urban areas.

This uniform nationwide correction method was insufficient, especially for Hi-net boreholes with many observation points in non-urban areas. Regarding climate change in Japan over the past 100 years, Fujibe (2012) quantitatively assessed background (non-urban) and urban warming trends. According to this, the national average background (non-urban) daily mean temperature was estimated to be 0.88 °C per 100 year, reaching 2.08 °C per 100 year around large cities, where the warming trend increases with increasing population density (Table 2).

According to "Climate Change in Northeastern Japan" (JMA 2016), the temperature in Sendai, the largest city in Northeastern Japan, is 2.4 °C per 100 year, 1.9 °C per 100 year in Aomori, and 1.7 °C per 100 year in Morioka. In the non-urban areas, many areas rely on the records of the past 50 years, with Fukaura at 0.4 °C per 50 year and Miyako at 0.7 °C per 100 year. These results are in general agreement with those of Fujibe (2012).

Based on this model, we estimated the temperature increase over the past 100 years according to the population density around the boreholes, using the Regional Economic Analysis System (https://resas.go.jp/) operated by the Cabinet Office for data on population density as of 2005 (Table 2).

Table 2 Climate change parameters. Fujibe (2012) shows the rate of temperature increase over the past 100 years, evaluated according to population density

Population densities	℃/Century	N-station (Hi-net)
Non-urban area	0.88	4
$P < 300$ km^{-2}	1.00	11
$300 \leq P < 1000$ km^{-2}	1.10	38
$1000 \leq P < 3000$ km^{-2}	1.60	41
$P \geq 3000$ km^{-2}	2.08	36

The number of Hi-net observation points applicable to each case is also shown

Long-term near-surface temperature changes in subsurface thermal structure vary with lithology. Therefore, in this study, for the seven lithology models listed in Table 1, we evaluated the change in the geothermal gradient after 100 years of continuous increase in surface temperature, according to Jessop (1990). The parameters for the Quaternary sedimentary layers were taken from Miyakoshi and Uchida (2001). Of the seven lithology models, those using granite as the lithology and Quaternary sedimentary layers as the lithology are shown in Figs. 4a–f and 5a–f. Both show the initial temperature distribution and the temperature distribution 100 years after the surface temperature started to rise. For the temperature trend, five cases of 0.88 °C per 100 year, 1.00 °C per 100 year, 1.10 °C per 100 year, 1.60 °C per 100 year, and 2.08 °C per 100 year were prepared for each of the seven lithology models, based on Fujibe (2012). Thus, a total of 35 cases were considered in this study.

The calculation results show that in Japan, the impact of climate change on the subsurface temperature gradient is very large up to a depth of 100 m, and the degree of impact on the temperature gradient due to different rates of temperature increase is also very different.

Three types of temperature profile data for Hi-net boreholes were collected in this study. The first one is two deeper than 200 m depths less affected by the climate change in the recent 100 years described here. Therefore, these two borehole wells are not subject to correction for climate change. Next are the temperature data for standard boreholes with 100 to 200 m depths. There are two sampling intervals for the temperature logging data here, one with a dense sampling interval of 1 m or 0.5 m (9 boreholes) and the other with a coarse sampling interval of 5 m (121 boreholes). For the former nine boreholes, we first tried fitting the observed T–D curve to the T–D curve calculated based on the temperature gradient of the initial conditions and the estimated temperature increase rate. The temperature gradient was arbitrarily assumed in 0.5 K km^{-1} units, and the fitting temperature gradient was selected by visual inspection.

For the latter 121 boreholes (115 boreholes excluding the 6 Class-D boreholes) that were coarsely sampled at 5-m intervals, a simple correction method was adopted because it was challenging to fit them using the same method as above.

Figures 4g–k and 5g–k show the ratio of the temperature gradient after 100 years from the initial condition for the five sections (60–80 m, 80–100 m, 100–120 m, 130–150 m, 180–200 m) in Figs. 4a–f and 5a–f. The temperature gradient ratios before and after 100 years in Fig. 4g–k for stations where the lithology is granite and Fig. 5g–k for stations where the lithology is Quaternary sedimentary formation were used as climate change

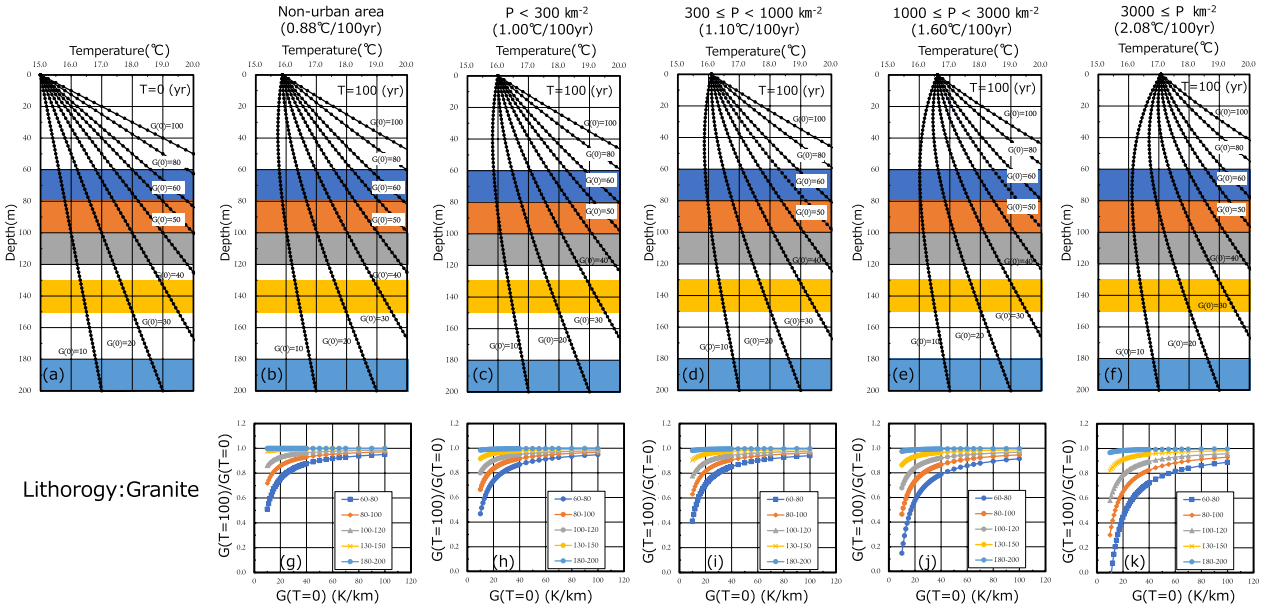

Fig. 4 Assessing the impact of climate change on temperature gradients at different depths. Changes in temperature profile associated with climate change. Lithology is granite. Temperature gradients are shown in 8 cases: 10 K km^{-1}, 20 K km^{-1}, 30 K km^{-1}, 40 K km^{-1}, 50 K km^{-1}, 60 K km^{-1}, 80 K km^{-1}, and 100 K km^{-1}. **a** The initial condition, and **b**, **c**, **d**, **e**, and **f** show the condition after 100 years. Based on Fujibe (2012), the trend of temperature rise over the past 100 years is expressed using five cases (0.88 °C per 100 years, 1.00 °C per 100 years, 1.10 °C per 100 years, 1.60 °C per 100 years, and 2.08 °C per 100 years) according to population density. **g**, **h**, **i**, **j**, and **k** show the temperature gradient ratios after 100 years from the initial condition for these five cases. Calculations are performed for each of the five intervals (60–80 m, 80–100 m, 100–120 m, 130–150 m, 180–200 m) shown in **b**, **c**, **d**, **e** and **f**. If the observed temperature gradient is Gobs, the corrected temperature gradient is Gcor, the temperature gradient 100 years ago is $G(T=0)$, and the currently estimated temperature gradient is $G(T=100)$, then $G_{cor}=G_{obs}\times G(T=0)/G(T=100)$, the reciprocal of the y-axis in this figure multiplied by the observed temperature gradient

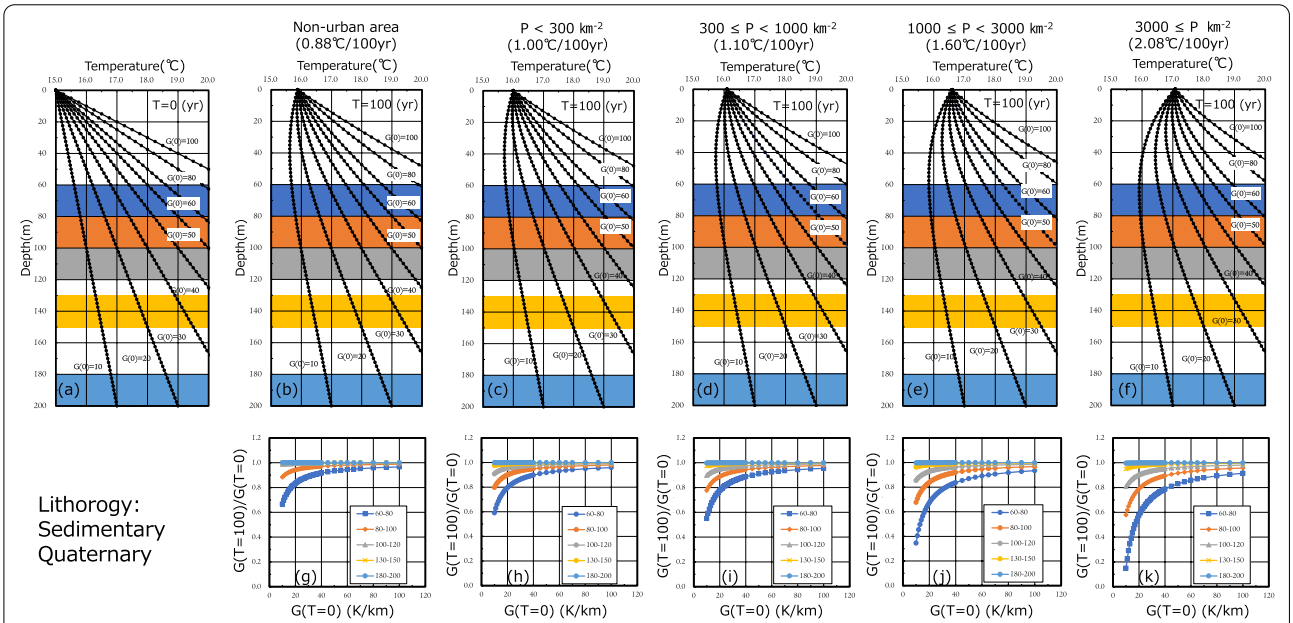

Fig. 5 Assessing the impact of climate change on temperature gradients at different depths. Changes in temperature distribution are associated with climate change. Lithology is Quaternary sediments. The composition of each figure is the same as in Fig. 4

correction factors for the measured temperature profiles. The other lithology sites were also classified into the remaining five lithologies listed in Table 1, and the temperature gradient ratios before and after 100 years were determined and used as correction factors.

In the case of the most common 100-m borehole, the average temperature gradient of the 80–100 m section is used for comparison, but the corrected temperature gradient is generally 5–20% larger. The error in the temperature gradient is calculated by multiplying the error in the temperature gradient before correction by the correction factor and is shown in Table 3. The larger the disturbance in the temperature profile due to groundwater and so on, the larger the error in the temperature gradient. The error is about 5% for Class-A boreholes, but for Class-B and Class-C boreholes, the error is about 10% and 10%, respectively (Fig. 6).

As we have discussed, we have attempted to correct for climate change with the model of Fujibe (2012). Here, we examine how the model is consistent with actual surface temperature rise over the past 100 years. Compared to JMA observations for each region in Northeastern Japan, there is a difference of about 0.3 °C, as mentioned above. In addition, a check of the temperature profiles of the Hi-net wells shows no significant temperature rise of more than 3.0 °C, which corresponds to a large city. If we allow an estimated range of temperature rise of up to 0.5 °C, we will attempt to calculate how much error we can expect. The effect of the different rates of temperature rise at the surface on the correction factor depends on the magnitude of the temperature gradient and which depth section was used in the analysis. In the 180–200 m section, the coefficient is less than 1% regardless of the magnitude of the temperature gradient; in the 130–150 m section, the coefficient is up to about 5% for temperature gradients below 25 K km^{-1} and less than 2% for gradients above 25 K km^{-1}. In the 80–100 m section, which is the most affected, the error in the temperature gradients is estimated to be ± 12% at 20 K km^{-1}, ± 7% at 30 K km^{-1}, ± 5% at 40 K km^{-1}, and ± 4% at 50 K km^{-1}. Errors of this magnitude could be further added to the temperature gradient errors shown in Table 3.

Heat flow map

Heat flow data at 126 stations were obtained by measuring temperature gradient values and thermal conductivities of rock cores. In addition, heat flow data of 65 stations were obtained by measuring the thermal conductivity of rock cores, and 61 stations were obtained by using lithology estimates shown in Table 1. The error in heat flow data is about 11% for Class-A, 15% for Class-B, and 12% for Class-C, due to this error in temperature gradient plus the measurement error in thermal conductivity measurement. A comparison with Matsumoto (2007), who assumed a uniform climate change correction of 2.0 °C increase in 100 years and estimated the thermal conductivity of rock cores at unmeasured sites from the average of surrounding stations, shows that the average value of the two is about 100 mW m^{-2}, which is not significantly different. However, when comparing the heat flow values for each borehole well, the heat flow in this study is 5% larger (Fig. 7). On the other hand, when restricted to boreholes with unmeasured thermal conductivity, the heat flow estimated from thermal conductivity based on Sato et al. (1999) and Gueguen and Palciauskas (1994) (Table 1) is about 14% larger in comparison.

In order to fill in the gaps in the distribution of Hi-net stations, the existing temperature logging data, Database on the Temperature Profiles of Boreholes in Japan (Sakagawa et al. 2004) (hereinafter referred to as DTPBJ), was examined for heat flow values, taking into account the geological conditions. However, because the DTPBJ includes many geothermal wells and hot spring wells in geothermal areas, many of these wells have been temperature logging immediately after drilling or not long enough after the temperature recovery test. The temperature recovery is not sufficient. Therefore, we extracted data only from these vertically drilled borehole wells, which are less affected by groundwater flow and exhibit good heat conductive type temperature profiles. The temperature gradient was determined when examining the heat flow by selecting the temperature profile section showing a straight line at the deep side. For high-temperature locations (above 100 °C), we attempted to correct the temperature dependence of thermal conductivity based on Miao et al. (2014) for granite and Funnell et al. (1996) for other lithologies when using the thermal conductivity of core samples registered in DTPBJ.

Although most of the 5000-m class boreholes drilled for resource exploration were not drilled vertically, Akiyama and Hirai (1997) estimated the vertical temperature gradient in these boreholes, which was adopted in this study. In addition, the government Ministry of International Trade and Industry (MITI) exploratory well Mishima, which is not included in the DTPBJ but was analyzed by Akiyama and Hirai (1997), was also analyzed in the same way as the DTPBJ. These results are shown in Table 4.

Figure 6 is a map of heat flow at the surface. Figure 6a plots the heat flow data for each measurement point, and Fig. 6b is plotted by interpolation using the nearest neighbor method. As shown in Fig. 6a, we obtained heat flow data over a large area of Northeastern Japan. There is a trend of less heat flow in the forearc, and more heat flow in the volcanic regions, and some regions have slightly

Table 3 Hi-net boreholes terrestrial heat flow

Site code	Site code (prefecture)	Latitude (N°)	Longitude (E°)	Elv (m)	Depth (m)	Interval (m)	Thermal gradient (K km^{-1})	Corrected gradient (K km^{-1})	σG (K km^{-1})	Thermal conductivity K (Wm^{-1} K^{-1})	σK (Wm^{-1} K^{-1})	Heat Flow Q (mW m^{-2})	σQ (mW m^{-2})	Bedrock depth (m)	Lithology	Age	Class	Population density	Measurement date
OOMH	AOMH01	41.5273	140.9127	13	103	80–100	80.0	85.3	4.3	(1.20)	0.24	102	21	1500	Shale/sandstone	Neogene	A	4	2000
SAIH	AOMH02	41.4049	140.8567	33	203	180–200	32.0	32.1	2.3	6.33	0.32	203	18	600	Shale	Neogene	A	2	2000
KUCH	AOMH03	41.2340	140.9896	23	103	80–100	86.0	89.1	2.1	(1.20)	0.24	107	22	1000	Pumice tuff	Neogene	A	2	2000
AOMH	AOMH04	40.8524	140.6759	13	310									2000	Sandstone	Quaternary	D	4	2000
NHJH	AOMH05	40.8564	141.1033	48	315	180–200	36.0	36.1	2.3	(1.62)	0.09	59	5	3000	Tuff	Neogene	C	3	2000
RKSH	AOMH06	40.9664	141.3738	8	103	80–100	36.0	39.5	2.5	(1.20)	0.24	47	10	3000	Sandstone	Neogene	A	3	2000
FKUH	AOMH07	40.7451	140.0233	43	112	100–120	66.0	67.9	2.1	(1.62)	0.09	110	7	500	Tuff	Neogene	A	2	2000
AJSH	AOMH08	40.7618	140.3121	53	163	140–160	62.0	62.5	3.1	(1.20)	0.24	75	15	2000	Sandstone	Neogene	A	2	2000
IKIH	AOMH09	40.6199	140.3499	163	165	145–165	66.0	66.1	5.0	(1.20)	0.24	79	17	2000	Tuff breccia	Quaternary	C	2	2000
KRIH	AOMH10	40.6091	140.6646	105	109	80–100	128.0	132.6	19.9	(1.20)	0.24	159	40	1000	Tuff	Neogene	B	3	2000
TWWH	AOMH11	40.5800	140.9950	243	103	80–100	82.0	83.2	3.1	1.94	0.10	162	10	2000	Andesite	Quaternary	C	1	2000
TWEH	AOMH12	40.5846	141.1547	88	103									3000	Sandstone	Neogene	D	3	2000
HHEH	AOMH13	40.5794	141.4451	13	153	130–150	36.0	36.4	6.2	(1.20)	0.24	44	11	3000	Sandstone	Quaternary	B	4	2000
NYAH	AOMH14	40.5488	140.2726	161	103	80–100	114.0	117.7	5.7	(1.62)	0.09	191	14	500	Tuff breccia	Neogene	A	2	2000
OWNH	AOMH15	40.4841	140.5565	133	103	80–100	74.0	79.0	7.7	(1.62)	0.09	128	14	200	Shale	Neogene	B	4	2000
SHGH	AOMH16	40.4624	141.0923	318	153	130–150	74.0	74.1	3.8	(1.20)	0.24	89	18	2000	Sandstone	Neogene	A	1	2000
NWAH	AOMH17	40.4492	141.3374	68	117	95–115	46.0	48.8	2.1	(1.56)	0.09	76	5	1000	Sandstone	Neogene	A	3	2000
TTKH	AOMH18	40.2962	141.0145	238	103	80–100	50.0	52.6	2.1	(1.56)	0.09	82	6	500	Sandstone	Neogene	A	1	2000
NSNH	AKTH01	39.8147	140.5790	321	103	80–100	86.0	88.5	2.1	(1.62)	0.09	143	9	1000	Mudstone	Neogene	A	1	2000
NSSH	AKTH02	39.6634	140.5721	98	103	80–100	56.0	59.5	2.5	(1.62)	0.09	96	7	1000	Tuff	Neogene	A	3	2000
YJMH	AKTH03	39.2223	140.1283	148	106	80–100	60.0	63.4	0.0	(1.20)	0.24	76	15	3000	Mudstone	Neogene	A	3	2000
HNRH	AKTH04	39.1740	140.7129	283	103	80–100	54.0	56.4	2.1	(1.62)	0.09	91	6	2000	Tuff breccia	Neogene	A	1	2000
CHKH	AKTH05	39.0718	140.3185	278	203	180–200	58.0	58.0	3.8	3.02	0.15	175	15	100	Andesite	Paleogene	A	1	2000
OGCH	AKTH06	38.9801	140.4952	288	103	80–100	110.0	113.6	3.2	(1.62)	0.09	184	11	100	Tuff breccia	Neogene	A	2	2000
KOSH	AKTH07	40.4563	140.8395	408	108	80–100	84.0	86.5	3.4	1.40	0.07	121	8	1000	Tuff breccia	Neogene	C	1	2000
FSTH	AKTH08	40.3188	140.2341	128	203	180–200	70.0	70.1	2.0	(1.56)	0.09	109	7	2000	Andesite	Neogene	A	2	2000
TSRH	AKTH09	40.2755	140.4596	48	104	80–100	64.0	67.6	2.4	(1.62)	0.09	110	7	1000	Mudstone	Neogene	A	3	2000
ODTH	AKTH10	40.3002	140.5812	88	103	80–100	72.0	76.9	4.9	1.29	0.06	99	8	600	Tuff breccia	Neogene	A	4	2000
OGAH	AKTH11	39.9554	139.7623	59	353	180–200	84.0	84.2	6.1	1.89	0.09	159	14	2000	Andesite	Paleogene	A	2	2000
GJOH	AKTH12	39.9155	140.2221	93	103	80–100	60.0	62.7	0.0	(1.20)	0.24	75	15	100	Mudstone	Neogene	A	1	2000
ANIH	AKTH13	39.9819	140.4072	148	103	80–100	64.0	67.3	6.4	2.69	0.13	181	19	500	Tuff	Paleogene	A	2	2000
KZNH	AKTH14	40.0622	140.8084	323	111	100–120	52.0	53.1	2.4	(1.62)	0.09	86	6	1000	Tuff	Neogene	A	1	2000
KWAH	AKTH15	39.6884	140.4075	168	103	80–100	50.0	52.7	2.1	3.42	0.17	180	12	100	Rhyolite	Neogene	A	1	2000
NSBH	AKTH16	39.5450	140.3481	28	157	130–150	82.0	82.7	3.9	(1.20)	0.24	99	20	2000	Sandstone	Neogene	A	2	2000
NSEH	AKTH17	39.5575	140.6116	98	180	155–175	62.0	62.1	3.1	(1.20)	0.24	75	15	2000	Sandstone	Quaternary	A	3	2000

Table 3 (continued)

Site code	Site code (prefecture)	Latitude (N°)	Longitude (E°)	Elv (m)	Depth (m)	Interval (m)	Thermal gradient (K km^{-1})	Corrected gradient (K km^{-1})	σG (K km^{-1})	Thermal conductivity K (Wm^{-1} K^{-1})	σK (Wm^{-1} K^{-1})	Heat Flow Q (mW m^{-2})	σQ (mW m^{-2})	Bedrock depth (m)	Lithology	Age	Class	Population density	Measurement date
OMRH	AKTH18	39.3548	140.3869	68	103	80–100	74.0	77.5	2.1	(1.20)	0.24	93	19	500	Tuff	Neogene	A	2	2000
YUZH	AKTH19	39.1913	140.4710	78	183	155–175	56.0	56.1	2.3	(1.20)	0.24	67	14	1000	Sandstone	Quaternary	A	4	2000
NHEH	IWTH01	40.2383	141.3423	233	203	180–200	46.0	46.1	3.8	(1.62)	0.09	77	12	500	Conglom-erate	Neogene	A	2	2000
TMYH	IWTH02	39.8250	141.3826	678	106	80–100	26.0	29.0	2.2	4.60	0.23	134	12	100	Slate	Jurassic	A	1	2000
IWZH	IWTH03	39.8020	141.6520	313	103	10–100		25.5	0.0	3.39	0.17	77	4	100	Diorite	Cretaceous	A	1	2000/2006
SMTH	IWTH04	39.1809	141.3909	623	109	80–100	20.0	22.8	0.0	2.70	0.13	61	3	100	Andesite	Cretaceous	A	1	2000
FSWH	IWTH05	38.8654	141.3512	123	103	75–95	14.0	18.6	2.7	2.85	0.14	53	8	100	Tonalite	Cretaceous	A	3	2000
NHWH	IWTH06	40.2611	141.1709	228	103	80–100	26.0	29.6	2.3	1.24	0.06	37	3	1000	Sandstone	Neogene	A	2	2000
KRMH	IWTH07	40.2705	141.5709	263	123	100–120	14.0	15.7	2.2	(3.19)	0.15	50	8	100	Sandstone	–	A	2	2000
KJNH	IWTH08	40.2686	141.7831	178	103	70–90	10.0	14.5	2.9	2.77	0.14	40	8	100	Granodi-orite	Cretaceous	A	3	2000
KJSH	IWTH09	40.0861	141.7120	243	103	80–100	10.0	13.4	2.7	2.55	0.13	34	7	100	Limestone	Cretaceous	A	2	2000
ASRH	IWTH10	40.1391	140.9529	311	103	80–100	30.0	32.6	2.2	2.44	0.12	79	7	500	Tuff breccia	Neogene	A	1	2000
IHEH	IWTH11	40.0811	141.1915	632	303	180–200	32.0	32.0	2.3	1.73	0.09	55	5	1000	Tuff	Quaternary	B	1	2000
KHEH	IWTH12	40.1533	141.4245	368	103					6.65	0.33			100	Slate	Quaternary	D	2	2000
KZMH	IWTH13	39.9398	141.5492	573	120	100–120	6.0	8.6	2.9	(6.60)	0.33	57	19	100	Slate	Paleozoic era ?	A	1	2000
TROH	IWTH14	39.7435	141.9087	203	103	10–100		17.5	0.0	2.71	0.14	47	2	100	Granodi-orite	Cretaceous	A	1	2000/2006
YHBH	IWTH15	39.6148	141.0929	198	125	100–120	34.0	36.7	4.1	(1.62)	0.09	59	7	1000	Tuff breccia	Neogene	A	3	2000
SZKH	IWTH16	39.6436	140.9465	215	153	130–150	50.0	50.8	2.0	1.24	0.06	63	4	1000	Tuff breccia	Neogene	A	3	2000
KANH	IWTH17	39.6442	141.5977	308	106	10–100		15.0	0.0	7.37	0.37	111	6	100	Slate	Paleozoic era ?	A	2	2000/2006
KASH	IWTH18	39.4630	141.6775	555	103	10–100		23.0	0.0	2.47	0.12	57	3	100	Hornfels	Paleozoic era ?	A	1	2000/2006
HMNH	IWTH19	39.4559	141.0001	223	104	85–105	138.0	141.7	23.1	1.34	0.07	190	32	2000	Tuff breccia	Neogene	A	1	2000
HMSH	IWTH20	39.3434	141.0473	109	159	135–155	74.0	74.9	5.6	(1.20)	0.24	90	19	2000	Mudstone	Neogene	A	3	2000
YMDH	IWTH21	39.4734	141.9336	16	103	10–100		18.5	0.0	2.65	0.13	49	2	100	Granite	Cretaceous	A	3	2000/2006
TOUH	IWTH22	39.3340	141.3015	263	103	80–100	26.0	29.4	4.3	3.23	0.16	95	15	100	Granodi-orite	Cretaceous	A	2	2000
KMIH	IWTH23	39.2741	141.8233	47	106	10–100		20.5	0.0	3.11	0.16	64	3	100	Shale	Paleogene	A	4	2000/2006
KGSH	IWTH24	39.1979	141.0118	203	153	130–150	78.0	78.7	3.9	0.97	0.05	76	5	2000	Sandstone	Neogene	A	2	2000
ICWH	IWTH25	39.0092	140.8638	389	263	180–200	90.0	90.0	2.0	1.95	0.10	175	10	2000	Tuff breccia	Neogene	A	1	2000
ICEH	IWTH26	38.9690	141.0013	128	111	90–110	48.0	50.4	4.2	2.10	0.10	106	10	2000	Andesite	Neogene	A	2	2000

Table 3 (continued)

Site code	Site code (prefecture)	Latitude (N°)	Longitude (E°)	Elv (m)	Depth (m)	Interval (m)	Thermal gradient (K km^{-1})	Corrected gradient (K km^{-1})	σG (K km^{-1})	Thermal conductivity K (Wm^{-1} K^{-1})	σK (Wm^{-1} K^{-1})	Heat Flow Q (mW m^{-2})	σQ (mW m^{-2})	Bedrock depth (m)	Lithology	Age	Class	Population density	Measurement date
RZTH	IWTH27	39.0307	141.5320	83	103	85–105	14.0	17.2	2.5	2.84	0.14	49	7	100	Tuff	Carboniferous ?	A	2	2000
TDOH	YMTH01	38.3841	140.3805	116	210	180–200	202.0	202.0	15.1	(1.20)	0.20	242	52	2000	Tuff	Neogene	B	5	2000
YGTH	YMTH02	38.2693	140.2583	133	153	115–135	46.0	46.7	4.7	(1.20)	0.24	56	13	2000	Conglomerate	Neogene	B	3	2000
NYOH	YMTH03	38.1035	140.1553	281	117	95–115	34.0	36.0	4.1	2.61	0.13	94	12	100	Granite	Cretaceous	A	1	2000
KMYH	YMTH04	38.0813	140.2978	318	103	80–100	60.0	62.7	0.0	2.35	0.12	147	7	1000	Tuff	Neogene	B	1	2000
ONIH	YMTH05	37.9883	139.8017	283	110	85–105	66.0	69.1	2.1	2.30	0.11	159	9	2000	Tuff	Paleogene	A	2	2000
THTH	YMTH06	37.9633	140.1836	236	148	125–145	56.0	57.1	2.4	(1.62)	0.09	93	6	1000	Tuff	Paleogene	A	3	2000
YNZH	YMTH07	37.8960	140.0278	355	203	180–200	50.0	50.1	3.1	(1.62)	0.09	81	7	1000	Tuff breccia	Paleogene	B	3	2000
YWTH	YMTH08	38.9701	140.0333	118	109	85–105	58.0	61.1	3.2	(1.20)	0.24	73	15	1000	Sandstone	Neogene	A	2	2000
TZWH	YMTH09	38.7498	140.1780	68	203	180–200	66.0	66.1	2.0	(1.56)	0.09	103	7	2000	Mudstone	Neogene	A	2	2000
FGTH	YMTH10	38.7107	140.3744	108	207	180–200	44.0	44.1	6.1	2.15	0.11	95	14	3000	Mudstone	Neogene	B	2	2000
MGMH	YMTH11	38.7132	140.5544	256	112	90–110	144.0	147.6	3.3	(1.20)	0.24	177	36	2000	Sandstone	Neogene	A	2	2000
TCKH	YMTH12	38.6357	140.0055	323	206	180–200	66.0	66.0	2.0	(1.56)	0.09	103	7	2000	Mudstone	Neogene	A	1	2000
ASAH	YMTH13	38.4704	139.7606	268	107	85–105	36.0	38.5	6.5	2.23	0.11	86	15	1000	Mudstone	Neogene	B	1	2000
NKWH	YMTH14	38.3860	139.9916	468	106	80–100	64.0	67.2	10.6	(1.20)	0.24	81	21	1000	Mudstone	Neogene	B	2	2000
NKEH	YMTH15	38.4257	140.1249	308	103	80–100	40.0	42.6	3.5	1.80	0.09	77	7	1000	Mudstone	Neogene	B	1	2000
SNDH	MYGH01	38.2400	140.9969	32	1236	900–1100	24.9	-	0.2	(3.19)	0.15	79	4	1000	Sandstone	Triassic	A	-	2008
NRKH	MYGH02	38.8587	140.6513	348	206	100–200	80.0	80.0	4.0	3.16	0.16	253	18	100	Green schist	Paleozoic era ?	C	1	2000
KKWH	MYGH03	38.9207	141.6377	53	120	10–100		23.0	0.0	3.32	0.17	76	4	100	Slate	Paleogene	B	2	2000/2006
TOWH	MYGH04	38.7860	141.3254	38	103	80–100	16.0	19.0	2.7	3.41	0.17	65	10	100	Slate	Paleogene	A	1	2000
ONDH	MYGH05	38.5793	140.7804	62	340	180–200	92.0	92.1	2.3	(1.20)	0.24	111	22	1500	Sandstone	Neogene	A	3	2000
TAJH	MYGH06	38.5907	141.0710	23	103	80–100	60.0	63.7	4.2	1.01	0.05	65	5	1500	Sandstone	Neogene	B	3	2000
KWSH	MYGH07	38.1802	140.6405	189	145	125–145	86.0	87.4	13.8	(1.20)	0.24	105	27	500	Sandstone	Neogene	B	3	2000
IWNH	MYGH08	38.1133	140.8441	13	103	80–100	52.0	60.6	2.7	0.74	0.04	45	3	2000	Conglomerate	Neogene	A	5	2000
SISH	MYGH09	38.0091	140.6027	133	103	180–200	70.0	70.0	2.0	1.49	0.07	105	6	1000	Sandstone	Neogene	A	3	2000
YMMH	MYGH10	37.9411	140.8924	21	208	180–200	54.0	54.2	2.0	1.08	0.05	59	4	1000	Sandstone	Neogene	A	3	2000
KAKH	MYGH11	38.5158	141.3421	8	210	20–200		22.5	0.0	3.35	0.17	75	4	100	Schist	Triassic	A	2	2001/2006
SZGH	MYGH12	38.6416	141.4428	21	106	85–105	16.0	19.4	2.8	3.11	0.16	60	9	100	Shale/sandstone	Triassic	A	2	2001
MSRH	MYGH13	38.6993	141.4176	103	103	10–100		24.5	0.0	(2.68)	0.13	66	3	100	Shale	Cretaceous	A	3	2013

Table 3 (continued)

Site code	Site code (prefecture)	Latitude (N°)	Longitude (E°)	Elv (m)	Depth (m)	Interval (m)	Thermal gradient (K km^{-1})	Corrected gradient (K km^{-1})	σG (K km^{-1})	Thermal conductivity (Wm^{-1} K^{-1})	σK (Wm^{-1} K^{-1})	Heat Flow Q (mW m^{-2})	σQ (mW m^{-2})	Bedrock depth (m)	Lithology	Age	Class	Population density	Measurement date
RIFH	MYGH14	38.3400	140.9551	1065	1065	950–1000	30.5	-	0.5	(2.68)	0.13	82	4	500	Shale	Cretaceous	A	-	2013
NAZH	FKSH01	37.7565	139.7150	441	103	80–100	56.0	59.3	3.5	5.27	0.26	313	24	100	Granite	Cretaceous	A	1	2000
ATKH	FKSH02	37.7317	139.8821	333	103	80–100	106.0	109.8	2.1	1.88	0.09	207	11	500	Mudstone	Neogene	A	3	2000
TSTH	FKSH03	37.6078	139.7533	228	130	80–100	66.0	69.1	2.1	(1.56)	0.09	108	7	1000	Sandstone	Neogene	A	2	2000
ATDH	FKSH04	37.4508	139.8126	281	271	180–200	24.0	24.0	2.3	(1.20)	0.24	29	6	2000	Tuff breccia	Quaternary	B	2	2000
SMGH	FKSH05	37.2544	139.8725	499	108	80–100	42.0	45.5	6.5	(1.62)	0.09	74	11	500	Tuff	Neogene	A	3	2000
INAH	FKSH06	37.1723	139.5199	575	103	80–100	56.0	59.1	8.1	2.97	0.15	176	26	2000	Tuff breccia	Neogene	B	2	2000
HMTH	FKSH07	37.0103	139.3755	977	203	125–145	60.0	61.6	0.0	2.68	0.13	165	8	100	Sandstone	Paleogene	B	1	2000
NNMH	FKSH08	37.2822	140.2144	346	108	80–100	50.0	52.3	2.1	1.88	0.09	98	6	1500	Tuff breccia	Quaternary	A	3	2000
KRYH	FKSH09	37.3530	140.4264	263	203	80–100	34.0	40.0	2.4	3.41	0.17	136	11	100	Welded tuff	Quaternary	A	5	2000
NGUH	FKSH10	37.1616	140.0930	568	204	180–200	82.0	82.1	3.8	1.52	0.08	125	9	500	Tuff breccia	Neogene	B	3	2000
YBKH	FKSH11	37.2006	140.3386	289	118	90–110	94.0	97.8	2.1	(1.62)	0.09	158	9	1000	Tuff	Neogene	A	4	2000
HTAH	FKSH12	37.2169	140.5703	473	108	85–105	20.0	23.4	0.0	2.73	0.14	64	3	100	Granodi-orite	Cretaceous	A	2	2000
IWWH	FKSH13	36.9951	140.5853	583	108	75–95	18.0	21.2	2.4	(3.19)	0.15	68	8	100	Gneiss	Paleozoic era ?	B	2	2000
IWEH	FKSH14	37.0264	140.9702	6	150	125–145	30.0	31.1	2.1	2.32	0.12	72	6	3000	Sandstone	Neogene	A	3	2000
INWH	FKSH15	37.6461	140.1735	760	103	80–100	52.0	54.6	2.4	2.67	0.13	146	10	100	Tuff breccia	Neogene	B	1	2000
FKSH	FKSH16	37.7643	140.3766	138	303	180–200	68.0	68.0	4.0	1.92	0.10	130	10	500	Tuff breccia	Neogene	B	3	2000
KMAH	FKSH17	37.6636	140.5974	208	103	80–100	30.0	33.6	2.2	2.82	0.14	95	8	100	Granite	Cretaceous	A	3	2000
MRUH	FKSH18	37.4894	140.5380	413	103	80–100	24.0	27.6	2.7	2.94	0.15	81	9	100	Granite	Cretaceous	A	3	2000
MKJH	FKSH19	37.4703	140.7227	513	103	60–80	16.0	21.4	2.7	2.32	0.12	50	7	100	Granite	Cretaceous	B	2	2000
NMEH	FKSH20	37.4911	140.9871	15	112	85–105	42.0	47.2	3.4	(1.20)	0.24	57	12	1000	Sandstone	Neogene	B	4	2000
TDMH	FKSH21	37.3421	139.3147	378	203	180–200	66.0	66.1	2.0	2.73	0.14	180	11	100	Tuff	-	A	2	2000
NGOH	NIGH01	37.4272	138.8876	88	103	Not yet measured								4000	Sandstone	-			
AHIH	NIGH02	38.2799	139.5486	37	108	70–90	42.0	46.6	5.1	(1.20)	0.24	56	13	1000	Sandstone	Neogene	B	2	2000
ARKH	NIGH03	38.1327	139.4289	9	224	180–200	44.0	44.0	2.3	(1.20)	0.24	53	11	3000	Sandstone	Quaternary	A	3	2000
SKWH	NIGH04	38.1313	139.5428	81	103	80–100	46.0	49.3	2.1	(1.20)	0.24	59	12	1000	Mudstone	Neogene	A	3	2000
SROH	NIGH05	37.9759	139.2788	12	150	100–150	46.2	47.6	15.0	(1.20)	0.24	57	21	4000	Sandstone	Neogene	B	4	2000
KMOH	NIGH06	37.6527	139.0676	33	103	70–90	34.0	42.9	7.7	(1.20)	0.24	52	14	4000	Sandstone	Neogene	B	5	2000
MRMH	NIGH07	37.6658	139.2610	78	110	90–110	50.0	52.3	6.3	(2.68)	0.13	140	18	100	Shale	Cretaceous	A	1	2000
TWAH	NIGH08	37.6708	139.4648	71	303	80–100	66.0	69.8	14.4	1.09	0.05	76	16	1000	Tuff	Neogene	A	3	2000

Table 3 (continued)

Site code	Site code (prefecture)	Latitude (N°)	Longitude (E°)	Elv (m)	Depth (m)	Interval (m)	Thermal gradient (K km^{-1})	Corrected gradient (K km^{-1})	σG (K km^{-1})	Thermal conductivity K (Wm^{-1} K^{-1})	σK (Wm^{-1} K^{-1})	Heat Flow Q (mW m^{-2})	σQ (mW m^{-2})	Bedrock depth (m)	Lithology	Age	Class	Population density	Measurement date
STDH	NIGH09	37.5386	139.1279	96	103	80–100	78.0	81.2	6.2	(1.62)	0.09	132	12	4000	Tuff	Neogene	A	2	2000
KMKH	NIGH10	37.5438	139.3648	221	103	50–100	46.4	46.4	4.6	(1.62)	0.09	75	9	1000	Tuff	Neogene	C	1	2000
KWNH	NIGH11	37.1728	138.7440	168	208	180–200				1.23	0.06			4000	Sandstone	Neogene	D	3	2000
YNTH	NIGH12	37.2239	138.9821	113	113	90–110	52.0	56.0	2.5	(1.20)	0.24	67	14	3000	Tuff	Quaternary	A	4	2000
MAKH	NIGH13	37.0544	138.3966	233	103	80–100	50.0	53.3	2.1	(1.62)	0.09	86	6	4000	Mudstone	Neogene	A	2	2000
SZWH	NIGH14	37.0303	138.8521	188	390	180–200	40.0	40.0	3.3	2.64	0.13	106	10	4000	Sandstone	Quaternary	B	3	2000
MUIH	NIGH15	37.0533	138.9951	361	103	80–100	24.0	26.8	2.6	2.97	0.15	80	9	100	Granite	Cretaceous	A	1	2000
IGWH	NIGH16	36.9378	137.8480	152	103	80–100	44.0	46.3	10.6	3.41	0.17	158	37	100	Gabbro	Paleogene	B	1	2000
MKGH	NIGH17	36.8569	138.0966	1308	153					1.91	0.10			1000	Andesite	-	D	1	2000
MKOH	NIGH18	36.9425	138.2594	243	113									1000	Sandstone	Quaternary	D	3	2000
YZWH	NIGH19	36.8114	138.7849	988	103	80–100	32.0	34.8	2.5	3.18	0.16	111	10	100	Granite	Neogene	A	1	2000

Temperature gradients, temperature gradient corrections, thermal conductivities, heat flow values, and their respective errors are listed for the Hi-net station data used in this study. The temperature gradients and thermal conductivities in parentheses, for which errors are not listed, are formal error-free estimates. Borehole geology is taken from the columnar map. The depth of base rock is from SDLCM (NIED 2019)

less heat flow in the back-arc. In the volcanic region of the Ou Backbone Range, the heat flow values are very different despite the close distance between the measurement points, suggesting that the influence of groundwater behavior is significant. The interpolated Fig. 6b shows that high heat flow areas are distributed along the Ou Backbone Range, while low heat flow areas are distributed on the front arc side, especially in the northern and southern parts of the Kitakami Mountains, the eastern part of Abukuma Mountains, and near the Niigata Plain on the back-arc side (see Fig. 6c).

Thermal structure

Method

Based on this study's heat flow data, 1-D steady-state conductive geotherms are computed using finite difference approximations (e.g., Beardsmore and Cull 2001). Previous studies that estimated crustal temperatures by one-dimensional heat conduction include Okubo et al. (1998) and Tanaka (2009). The 1-D heat conduction is shown in Eq. (1), where T is the temperature at depth z, λ is the thermal conductivity, and A is the crustal heat generation:

$$\frac{\partial}{\partial z}\left(\lambda\frac{\partial T}{\partial z}\right)+A=0. \tag{1}$$

Therefore, we need to know the constituent materials of the subsurface, thermal conductivity, and crustal heat generation. In this study, we adopted a model that incorporates current knowledge of the crustal structure of Northeastern Japan and takes into account the temperature dependence of the thermal conductivity of rocks. The crustal structure model used in this study is explained in section "Structure model". In addition, how the temperature dependence of thermal conductivity is treated is explained in section "Thermal conductivity". Finally, the crustal heat generation model is explained in section "Heat generation" (Fig. 9).

Structure model

In assuming the crustal structure model for Northeastern Japan, we followed the crustal structure model treated by Muto et al. (2013). We consider the lithospheric structure obtained from wide-angle reflection and seismic refraction profiles throughout Northeastern Japan (Iwasaki et al. 2001; Nishisaka et al. 2001; Ito et al. 2004; Takahashi et al. 2004). Following the petrological interpretation of the seismic structure of Northeastern Japan Arc by Nishimoto et al. (2005), we assume that the upper crust is granite, and the lower crust is hornblende-bearing gabbro. The thickness of the upper crust is assumed to be 18 km; according to Matsubara et al. (2017a), the depth of the Moho discontinuity is distributed between 30 and 35 km, so we set the Moho discontinuity at 30 km and calculate the temperature structure from the surface to 30 km (Model A). It has also been noted that some areas on the forearc side of Northeastern Japan have granite in the lower crust (Nishimoto et al. 2008; Ishikawa et al. 2014; Ishikawa 2017). Therefore, instead of a simple horizontal layer structure, we calculate a temperature structure with granite as the lower crust in the region shown in Fig. 9a (Model B).

In addition, there are plains with thick sedimentary layers and areas thickly covered with pyroclastic deposits in Northeastern Japan (e.g., Ozawa and Hirayama 1970; Ikebe et al. 1979; Yamanoi 2005; Kobayashi 1996; Tamanyu 2008). As shown in Table 1, the thermal conductivity of sedimentary layers is about half that of basement rocks. Therefore, to estimate the subsurface temperature structure of these areas, it is necessary to incorporate the sedimentary layers into the subsurface structure model. For this purpose, the shallow and deep layers combined model (SDLCM) (NIED 2019) was used to obtain the depth of the basement rock at each observation point and improve the accuracy of the temperature structure estimation.

Based on the lithologic information from the boreholes, five cases of tectonic models were created for Model A and Model B, respectively (Fig. 9b, c). Case A-1 and B-1 assume that the granite is exposed at the surface. In Case A-2, A-3, B-2, and B-3, where metamorphic and pre-Paleogene sedimentary rocks are exposed, we assume that the near-surface lithology continues up to 5 km below the surface, and granite is assumed below 5 km below the surface. In Case A-4 and Case B-4, the thickness of the Tertiary sedimentary layer is used as the estimated depth of the basement rock at the well location, and the depth below is assumed to be granite. Finally, in Case A-5 and Case B-5, where the bottom of the borehole is Quaternary sedimentary layers, the Quaternary sedimentary layers are assumed to be present up to a depth of 500 m, and the Tertiary sedimentary layers are assumed to be present from there to the estimated depth of the base rock, and the granite is assumed to be present below that.

Thermal conductivity

The thermal conductivity of rocks tends to decrease with increasing temperature (e.g., Cermak and Rybach 1982). Therefore, a model in which a simple linear function represents thermal conductivity and temperature is often used (Royer and Danis 1988; Bodri et al. 1989). On the

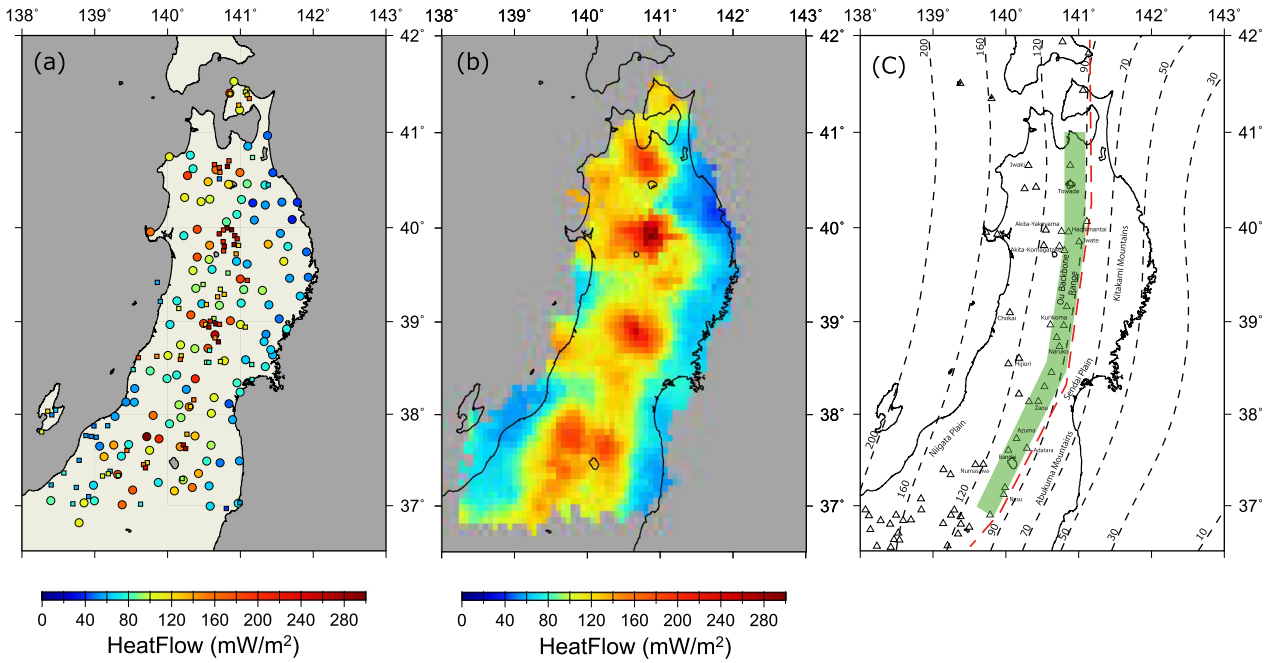

Fig. 6 Distribution of terrestrial heat flow. **a** Plots the heat flow rate at each measurement point. The circles indicate the heat flow at the Hi-net station, and the squares indicate the heat flow at the DTPBJ (Sakagawa et al. 2004). **b** Is plotted by interpolation using the Nearest neighbor method (nearest neighbor method). The grid size is set to 4 min. Triangles in **c** indicate volcanoes in Northeastern Japan. The red dashed line indicates the volcanic front (Yoshida et al. 2013). The green hatch area indicates the location of the Ou Backbone Range. Dashed continuous lines indicate depth (km) contours to the top of the subducted Pacific plate (PAC) slab (Iwasaki et al. 2015; Lindquist et al. 2004)

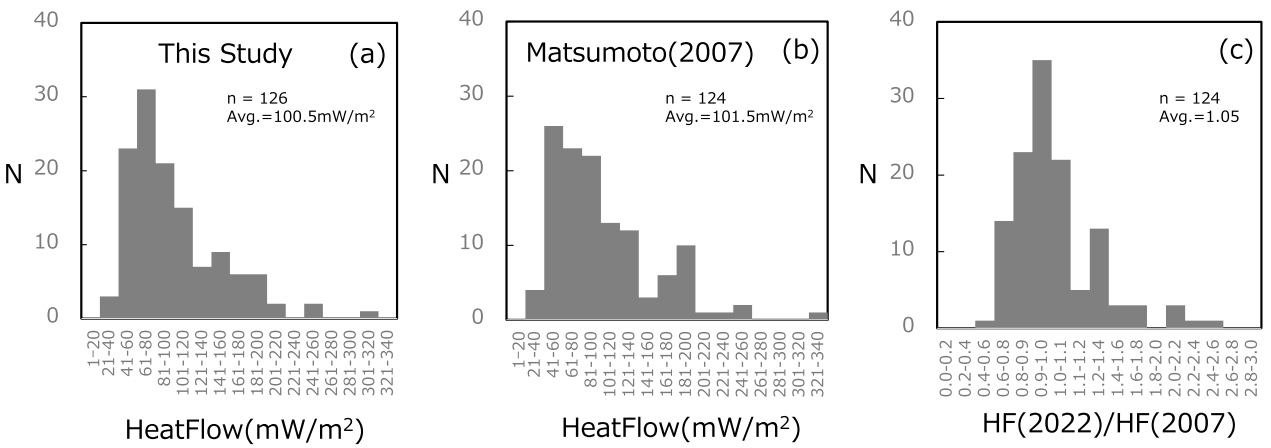

Fig. 7 Comparison of heat flow values between Matsumoto (2007) and this study. **a** The histogram of heat flow in this study. **b** A histogram of the heat flow in Matsumoto (2007). **c** The ratio of the heat flow estimated in Matsumoto (2007) to the heat flow estimated in this study for each borehole

other hand, to consider the large variability in the measured values, a model with a constant thermal conductivity in the upper crust is also used instead of a simple linear function model (Furukawa and Uyeda 1986; Tanaka 2009).

Miao et al. (2014) measured the thermal diffusivities and specific heat capacities of four types of rocks (granite, granodiorite, mafic rock, and hornblende) from room temperature to 1,173 K using the laser flash method and thermal analyzer simultaneously and then combined

Table 4 DTPBJ terrestrial heat flow

Site no.	Latitude (°E)	Longitude (°N)	Elv (m)	Depth (m)	Interval (m)	Thermal gradient (K km^{-1})	Thermal conductivity (Wm^{-1} K^{-1})	Heat flow (mW m^{-2})
438	41.4501	141.0870	160	1702	1200–1700	55	2.12	117
442	41.4207	141.0639	500	1492	750–1100	60	1.62	97
443	41.4026	140.8548	13	1000	400–600	39	(2.86)	112
444	41.3904	141.0895	35	1007	600–950	71	1.72	122
445	41.3540	141.1189	99	1503	1000–1500	70	2.37	165
446	41.2860	140.9742	91	1302	500–800	57	(2.36)	134
448	40.7402	141.1631	31	1001	500–1000	56	(1.56)	88
450	40.7052	140.8395	571	1000	800–1000	90	2.05	183
455	40.6666	140.6395	645	1501	1100–1500	113	1.75	197
458	40.6471	140.8181	733	1000	600–1000	129	2.59	334
461	40.6355	140.7070	250	503	300–500	102	1.89	193
462	40.5858	140.7157	100	1202	800–1200	83	1.86	154
470	40.5163	140.7084	356	1505	1000–1500	31	(1.62)	51
471	40.4527	141.3798	30	1123	600–1000	41	(1.62)	67
479	40.0002	140.8129	869	502	300–500	185	1.57	290
491	39.9808	140.8751	1,120	802	500–800	207	(2.76)	571
494	39.9789	140.7646	1,040	1701	1100–1700	94	(2.02)	190
498	39.9377	140.7057	490	1505	1000–1500	83	2.93	243
504	39.9186	140.9198	873	1002	800–1000	128	1.97	252
511	39.8847	140.9521	731	1004	700–900	164	1.39	228
514	39.8556	140.7604	551	2002	1700–2000	74	2.91	214
518	39.8245	140.9109	955	1503	1250–1490	193	(2.13)	410
520	39.8159	140.9718	707	1203	1000–1200	93	1.32	123
524	39.8047	140.7749	630	1501	1000–1500	72	3.66	263
532	39.7570	140.7654	710	1,501	1000–1500	75	2.69	202
534	39.7261	140.9379	462	1005	800–1000	135	1.03	139
536	39.5223	140.8271	410	1470	1100–1300	28	2.34	66
538	39.4438	141.0907	250	501	400–500	149	1.37	204
540	39.4195	139.8589	− 143	4800	3800–4600	25	(2.34)	58
541	39.4003	140.4835	30	850	600–850	49	(1.92)	94
543	39.3501	140.7210	250	1501	1000–1500	48	2.13	102
546	39.2945	140.7743	280	402	300–400	83	1.57	130
549	39.2687	140.6835	350	1004	800–1000	60	2.27	135
553	39.2195	139.8966	5	703	400–703	42	(1.45)	61
554	39.1862	140.5299	350	1002	800–1000	62	(2.08)	129
555	39.1437	140.1505	420	486	400–473.2	46	(2.14)	99
558	39.0368	140.6332	265	1004	750–1000	56	1.66	94
565	39.0085	140.5822	483	1803	1500–1800	103	(2.08)	213
586	38.9790	140.6588	640	1501	1000–1500	115	3.01	347
589	38.9740	140.7096	670	1202	1000–1200	134	1.49	199
591	38.9732	140.5191	330	1501	1000–1500	62	1.97	123
601	38.9448	140.5618	480	1032	800–1000	124	2.15	266
602	38.9446	141.0632	105	1100	800–1000	68	(1.83)	124
603	38.8287	140.6488	335	1500	1000–1450	94	1.51	142
616	38.7857	140.6946	307	1500	100–1500	132	2.77	366
623	38.6951	140.5721	325	1304	1000–1300	44	1.83	80
625	38.6356	140.1833	381	1502	1000–1500	81	1.50	122
626	38.6307	139.8494	70	1310	1150–1280	52	(2.83)	146

Table 4 (continued)

Site no.	Latitude (°E)	Longitude (°N)	Elv (m)	Depth (m)	Interval (m)	Thermal gradient ($K\ km^{-1}$)	Thermal conductivity ($Wm^{-1}\ K^{-1}$)	Heat flow ($mW\ m^{-2}$)
630	38.6154	139.5955	14	503	300–500	98	1.93	188
637	38.5974	140.1716	309	1802	1500–1800	82	2.16	176
640	38.5738	140.7218	180	1300	1000–1300	63	(1.67)	106
642	38.5654	140.5321	230	1703	1500–1700	46	2.24	102
643	38.5651	140.5621	470	1360	1000–1350	56	1.36	76
647	38.5418	141.1521	4	1000	100–1000	44	(1.83)	81
648	38.4860	139.5242	10	1300	100–1300	41	(1.83)	76
649	38.3775	141.1603	6	1700	1500–1700	34	(2.36)	80
650	38.1590	140.3566	545	801	500–800	73	2.25	164
652	38.0863	140.3105	295	501	300–500	36	3.32	120
653	38.0482	138.4596	10	1000	800–1000	36	1.83	66
654	38.0363	138.3524	72	1105	1015–1105	49	2.53	124
656	37.9965	138.4071	22	1300	1100–1300	30	1.77	53
657	37.8780	139.1734	3	4920	-	35	1.62	57
658	37.8757	138.9854	3	5007	-	32	1.62	51
662	37.8113	138.2691	30	1200	1000–1200	61	1.66	101
669	37.7861	140.2630	799	1303	1000–1500	62	(2.22)	137
672	37.7711	138.8754	4	6310	-	29	1.91	55
674	37.7621	138.9487	1	5015	-	32	1.62	52
675	37.7530	139.0165	2	4903	-	33	1.62	53
679	37.6683	140.2128	1000	1301	1000–1300	115	2.34	268
685	37.6291	140.2455	1100	1502	1000–1500	142	1.94	275
688	37.6086	139.4384	120	700	500–700	65	2.50	163
689	37.4750	139.7187	490	491	300–490	101	1.10	111
693	37.4530	139.6667	475	1005	600–1000	85	1.87	159
704	37.4189	139.6939	411	1800	1000–1800	93	2.58	239
705	37.3811	139.2076	575	800	600–800	29	(2.29)	65
706	37.3619	138.5729	2	853	600–800	34	(2.34)	78
707	37.3539	139.1823	560	1200	1000–1200	45	2.29	103
708	37.3350	139.3187	590	1300	1000–1300	53	(1.67)	89
709	37.3289	139.1034	450	1200	1000–1200	48	(2.15)	102
710	37.3003	140.1967	415	1200	800–1200	50	(1.83)	92
713	37.2302	138.3974	7	3781	–	37	(1.62)	60
716	37.2030	138.7440	297	4500	–	36	(1.62)	59
718	37.1031	138.9129	90	1200	1000–1200	23	(2.37)	55
720	37.0319	140.9944	5	1507	1000–1507	25	(2.14)	54
721	37.0225	138.6968	50	1500	900–1300	42	(1.83)	77
722	37.0197	139.6251	780	1002	750–1000	34	(2.13)	72
728	36.9714	140.8036	30	1151	900–1055	19	(2.18)	41
Mishima	37.5008	138.7819	5	6300	–	34	(1.62)	54

Adapted from Terrestrial Heat Flow on Database on the Temperature Profiles of Boreholes in Japan (DTPBJ) (Sakagawa et al. 2004). The depths used to calculate the temperature gradients are listed. The numbers in round brackets indicate estimated values in the thermal conductivity values. The latitude and longitude values of DTPBJ were converted to WGS-84 Datum assuming the Japan Geodetic System (Tokyo Datum) in the original paper, considering the geodetic system and the timing of acquisition of the original data is not mentioned in this paper

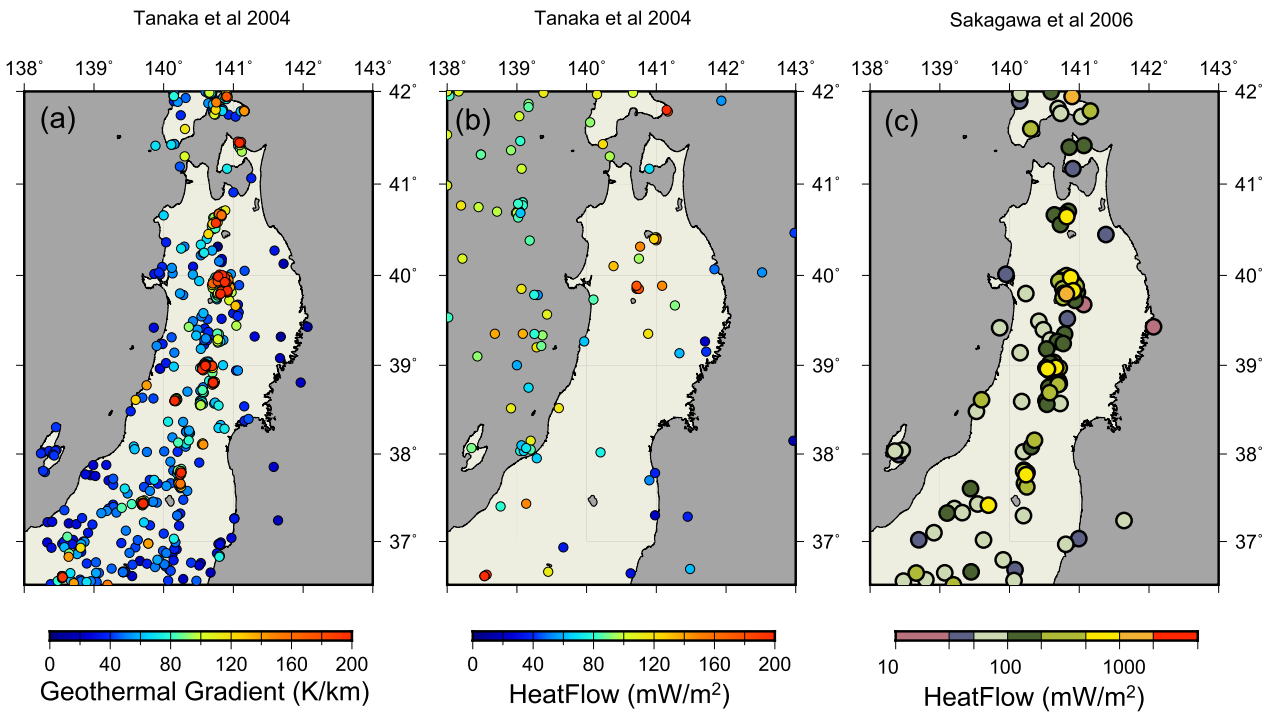

Fig. 8 Temperature gradient and heat flow distribution in previous studies. **a** Distribution of thermal gradient compiled by Tanaka et al. (2004). **b** Distribution of heat flow compiled by Tanaka et al. (2004). **c** Distribution of heat flow estimated by Sakagawa et al. (2006)

them with density data to calculate the thermal conductivity. In this study, we use the results of Miao et al. (2014) for granite and gabbro, which require calculations, especially at high temperatures. For Case A-2 and B-2, the Paleogene sedimentary rocks, the values in Table 1 based on lithological information from the boreholes were used as room temperature thermal conductivity using the formula of Funnell et al. (1996), and the temperature dependence of thermal conductivity was considered. For Case A-3 and B-3 metamorphic rocks, the measured thermal conductivities in Table 3 were used as room-temperature values, and the temperature dependence of thermal conductivity was considered using the Funnell et al. (1996) equation. For Case A-4, A-5, B-4, and B-5, which include Tertiary and Quaternary sedimentary formations, the thermal conductivities in Table 1 are used, and the temperature dependence was not considered here (see Table 5).

Heat generation

Regarding the content of radioactive materials in rocks, which is necessary for estimating crustal heat generation, Minato (2005) conducted a detailed study on the concentration of U, K, and Th in soils in various parts of Japan. The difference between the data for soil and rock is not very large, and it is safe to assume that the relationship between U, K, and Th is reasonably well maintained even when soil is replaced by rock. Therefore, for rocks that make up the upper part of the earth's crust, such as

(See figure on next page.)

Fig. 9 Crustal structure models. **a** The blue region is the area where granite is present in the lower crust, as noted by Ishikawa (2017). The crustal structure of this region is Model B. The crustal structure of the other regions is Model A. The continuous dotted lines denote depth (km) contours to the top of the subducted PAC slab (Iwasaki et al. 2015; Lindquist et al. 2004). **b** The crustal structure of Model A is shown. The upper crust is granite, and the lower crust is gabbro. The thickness of the upper crust is 18 km, and the depth of the Moho discontinuity is 30 km. Five cases are assumed, depending on the type of rock exposed at the surface and the thickness of the sedimentary layers. The depth of the basement rocks is based on the Shallow and deep layers combined model (SDLCM) (NIED 2019). Rock thermal conductivity and crustal heating values are as noted. **c** The crustal structure of Model B is shown. The upper crust and lower crust are granite. As in Model A, five cases are assumed, depending on the type of rock exposed at the surface and the thickness of the sedimentary layer. **d** The crustal structures of Model C and Model D are shown. The crustal structure of Model C is based on Tanaka (2009). The thermal conductivity of the rock is assumed to be constant. The crustal structure model D is based on Okubo et al. (1998). The upper crust is granite, and the lower crust is gabbro. The thickness of the upper crust is 18 km, and the depth of the Moho discontinuity is 30 km. Rock thermal conductivity and crustal heating values are as noted

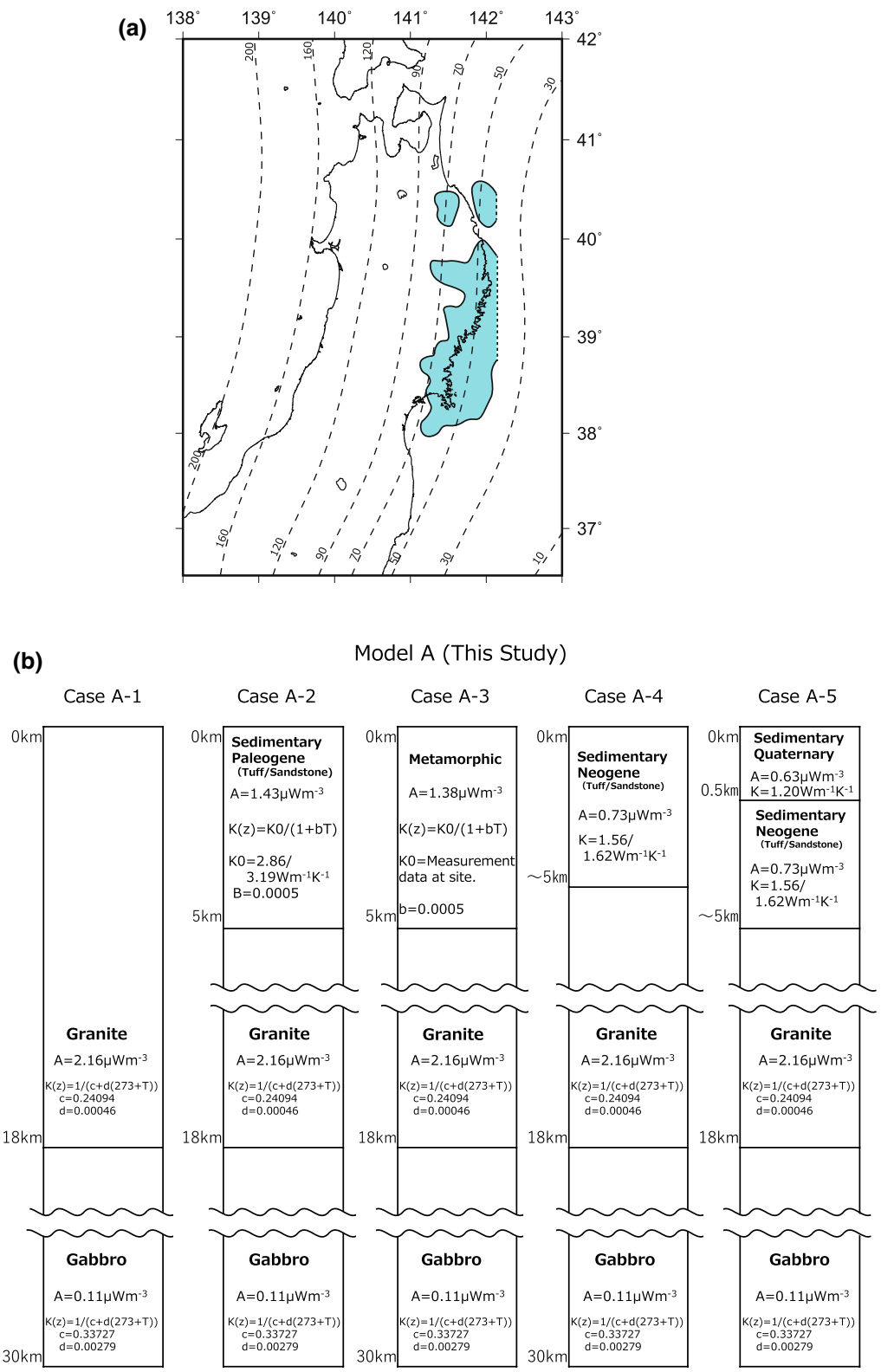

Fig.9 (See legend on previous page.)

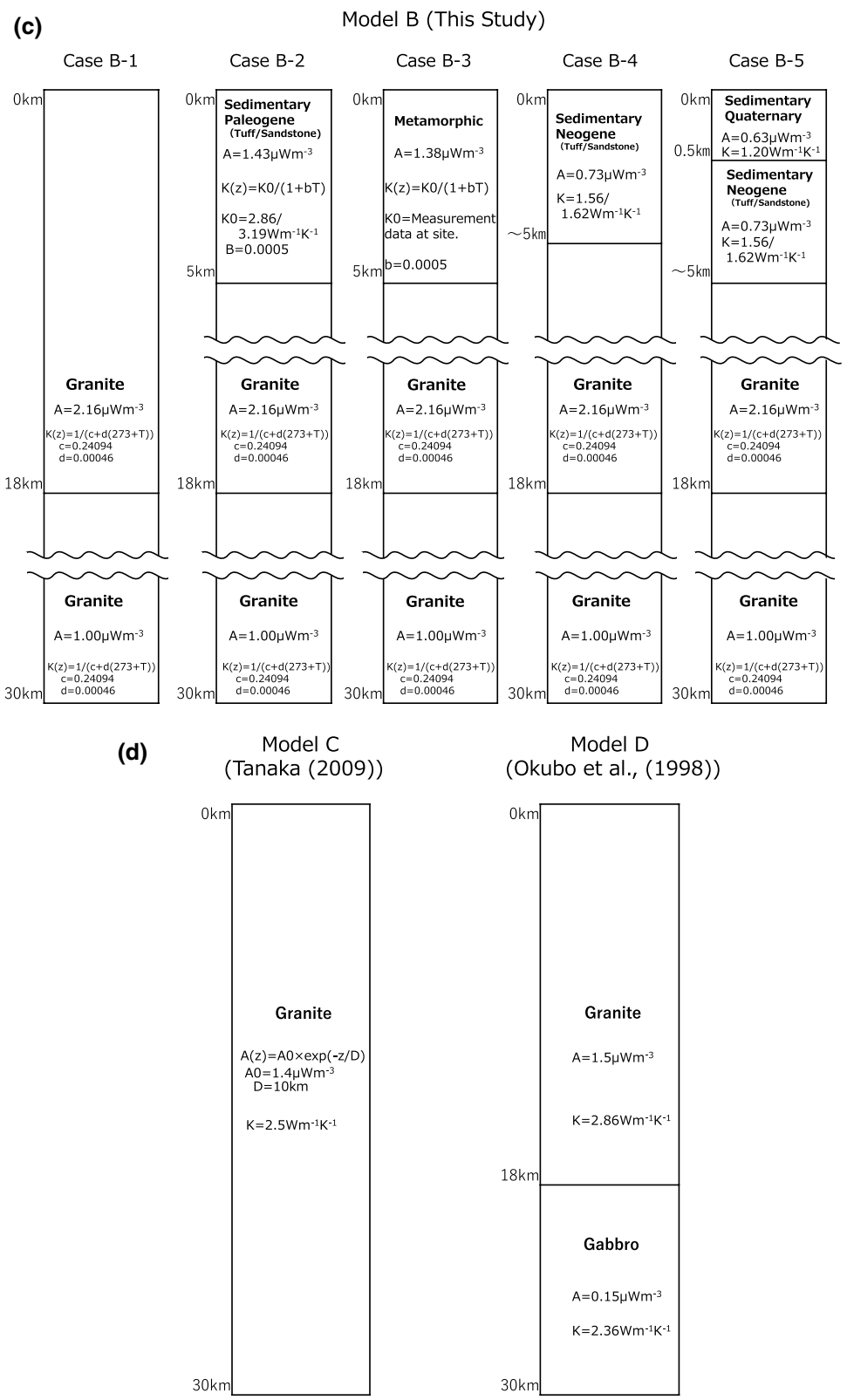

Fig. 9 continued

Table 5 Temperature dependence of thermal conductivity

Rock type	Thermal conductivity ($Wm^{-1}K^{-1}$)	
Granite	$K(T) = 1/(C + d \times (273.15 + T))$	$c = 0.24094$ $d = 4.6019 \times 10^{-4}$
Gabbro	$K(T) = 1/(C + d \times (273.15 + T))$	$C = 0.33727$ $d = 3.5002 \times 10^{-4}$
Other Bedrock	$K(T) = K(0)/(1 + b \times (T - 20))$	$b = 0.0005$

Based on Miao et al. (2014) for granite and gabbro. Based on Funnell et al. (1996), $K(0)$ indicates thermal conductivity at room temperature for other rocks

Table 6 Heat generation, A. Radiogenic heat value estimated based on Minato (2005). Based on Beardsmore and Cull (2001) for gabbro only

Rock type	Heat generation A ($\mu W\ m^{-3}$)
Granite	2.16
Gabbro and diorite	0.11(*)
Granodiorite	1.13
Rhyolite	1.23
Dacite	0.86
Andesite	0.77
Basalt	0.51
Metamorphic	1.38
Sedimentary Quaternary	0.63
Sedimentary Neogene	0.73
Sedimentary Paleogene	1.43

sedimentary layers and igneous rocks, we used this as a reference, and for gabbroic rocks that make up the lower part of the earth's crust, we estimated radiogenic heating based on Beardsmore and Cull (2001) (Table 6).

Two models have been proposed for heat generation in the earth's crust: one that decreases with depth (e.g., Furukawa and Uyeda 1986; Tanaka 2009) and one that varies from layer to layer (e.g., Erkan and Blackwell 2008; Okubo et al. 1998). This study adopts the layer model, defining multiple heating values depending on the crustal structure. Then, based on Eq. (2), the temperature T can be expressed as follows.

$$T = Ts + \frac{Q}{\lambda}z - \frac{A}{2\lambda}z^2 \tag{2}$$

Figure 10a shows the crustal structure model calculations in Model A (Case A-1) for seven cases with heat flow ranging from 50 to 200 mW m^{-2} in 25 mW m^{-2} increments. In the case of 75 mW m^{-2}, which is the average heat flow, the temperature reaches 300 °C at a depth of about 11 km, which seems reasonable compared to the depth of the seismogenic layer.

For comparison, we also calculated two models from previous studies (Fig. 9d): one is the structural model employed by Tanaka (2009), which assumes a constant thermal conductivity of 2.5 $Wm^{-1}\ K^{-1}$ and a crustal heat generation $A(z)$ that decreases exponentially with depth z:

$$A(z) = A(0)exp\left(-\frac{z}{D}\right). \tag{3}$$

Here, $D = 10$ km and heat generation at the surface $A(0) = 1.4\ \mu W\ m^{-3}$ (Model C).

The other is a structural model adopted by Okubo et al. (1998), in which the heat generation of the crust is assumed to be 1.5 $\mu W\ m^{-3}$ for the upper crust and 0.15 $\mu W\ m^{-3}$ for the lower crust. Thermal conductivity was estimated to be 2.5 $W\ m^{-1}\ K^{-1}$ for the upper crust and 2.0 $W\ m^{-1}\ K^{-1}$ for the lower crust, with lower values on the lower crust side to account for temperature dependence (Model D). Thermal structure calculations were performed for these two models (Fig. 10b and c).

In the shallow area of about 5 km, all three models do not differ much, but Model A tends to have a slightly higher temperature; for example, in the 100 mW m^{-2} calculation example, Model A is about 30 K warmer than Models C and D at 5 km. In the 200 mW m^{-2} calculation example, Model A has a temperature about 70 K higher than Models C and D at 5 km. As the heat flow increases, the temperature gradient increases, the temperature dependence of thermal conductivity becomes more pronounced, and the thermal conductivity decreases, further increasing the temperature gradient.

On the low heat flow side, in the case of 50 mW m^{-2}, the attenuation effect of heat flow due to radiogenic heating in the upper crust is significant. As a result, the temperature in the deep underground will be lower. However, as shown in Fig. 11, for example, when there is a thick sedimentary layer at the surface, the temperature gradient in the sedimentary layer increases, and the heat generated in the earth's crust decreases, so the heat flow does not decrease with increasing depth, and the temperature deep underground tends to be higher.

On the other hand, if granite is also present in the lower crust as in Model B, and the heat generation rates of the upper and lower crust are constant at, for example, 2.16 $\mu W\ m^{-3}$, the temperature gradient in the lower crust begins to reverse around 25 km depth when the surface heat flow is 55 mW m^{-2}. Therefore, referring to Furukawa and Uyeda (1986), we set the heat generation in the

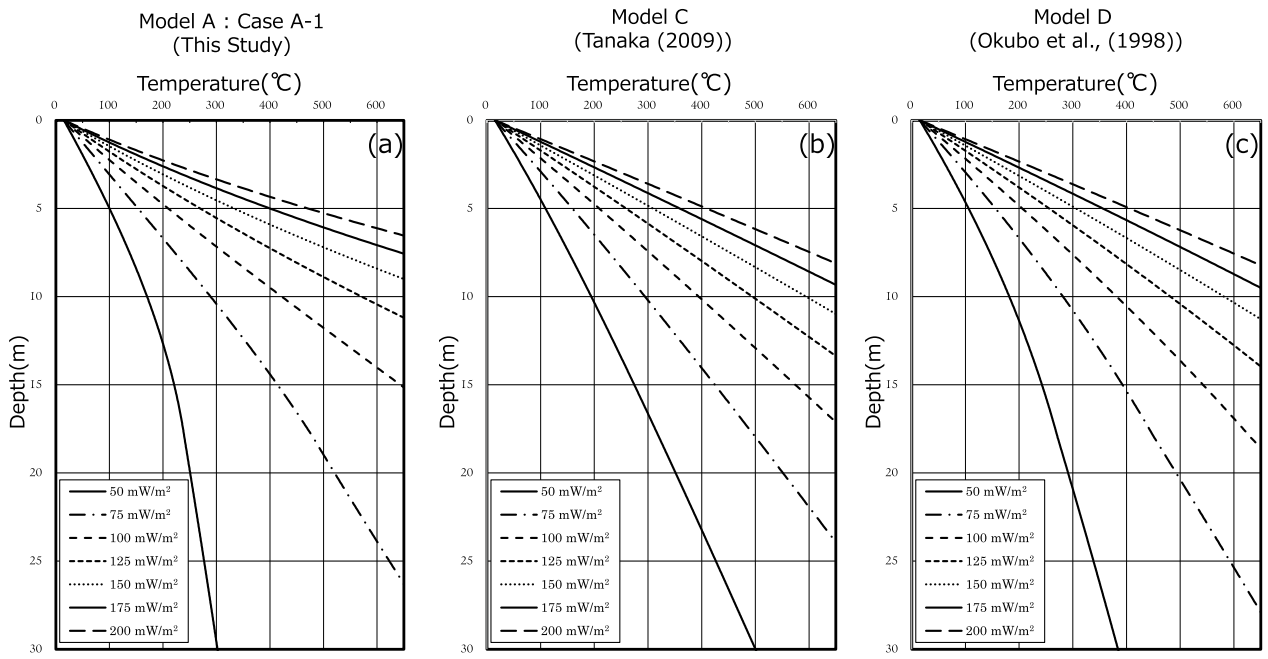

Fig. 10 Example of underground temperature calculation (1). The examples of calculations for seven cases with heat flow ranging from 50 to 200 mW m^{-2} in 25 mW m^{-2} increments. **a** Example calculation in Model A (Case A-1). **b** Example calculation in Model C. **c** Example calculation in Model D

lower crust, i.e., below a depth of 18 km, to 1.0 μW m^{-3}, which is almost the lower limit. If the surface heat flow is 50 mW m^{-2}, the temperature gradient becomes zero at a depth of 30 km. If the surface heat flow is 45 mW m^{-2}, the temperature gradient reverses at a depth of 23 km. However, at 30 km depth, the temperature is several K lower than the peak at 23 km depth (Fig. 12).

However, the heat flow measured in the relevant area in this study was below 50 mW m^{-2} in two wells, and the lowest value was around 47 mW m^{-2}. Therefore, although the temperature at 30 km depth will be about 5 K lower than the peak temperature, we decided to allow for this temperature drop in the present calculations based on the assumption that the results will be filtered to average the calculation results from multiple surrounding stations when discussing spatial distribution.

The heat flow values obtained estimate an error of 10–15%. The impact of this error on the estimation of subsurface temperature is estimated. In a typical case A-1 structural model with a heat flow of 50 mW m^{-2}, assuming an error of 5%, the range of estimated temperatures at 5 km below ground would be about ± 6 K, at 10 km below ground about ± 15 K, at 15 km about ± 23 K, and at 20 km below ground about ± 30 K. However, with an error of 15%, the estimated temperature range is about ± 16 K at 5 km below the surface, ± 34 K at 10 km below the surface, ± 50 K at 15 km below the surface, and ± 70 K at 20 km below the surface. Uncertainty is higher at deeper depths, reaching ± 110 K at 30 km. In the case of 75 mW m^{-2}, an error of 5% would result in ± 19 K at 10 km below ground, and an error of 15% would result in ± 50 K. In the case of 100 mW m^{-2}, the error of 5% would be ± 25 K at 10 km below the surface, and the error of 15% would be ± 80 K. Uncertainty tends to increase at shallow depths with high heat flow. Thus, the method of estimating crustal thermal structure assumed in this study is a model in which the estimated temperature distribution is more sensitive to differences in crustal structure than in previous studies.

Solidus temperature

The partial melting state above the solidus temperature, where the assumption of one-dimensional heat conduction does not hold, is considered as follows. In the upper crust, granitoid have solidus temperatures of 600–700 °C at depths greater than 10 km (Robertson and Wyllie, 1971). The temperature of the lower crustal constituents, such as hornblende and waterless gabbro, is estimated to be 800–900 °C (Tatsumi et al. 1994; Yoshida et al. 2005). Here, following the methods of Okubo et al. (1998) and Nishida and Hashimoto (2007), we assume that the temperature of the upper crustal solidus is 650 °C, the temperature of

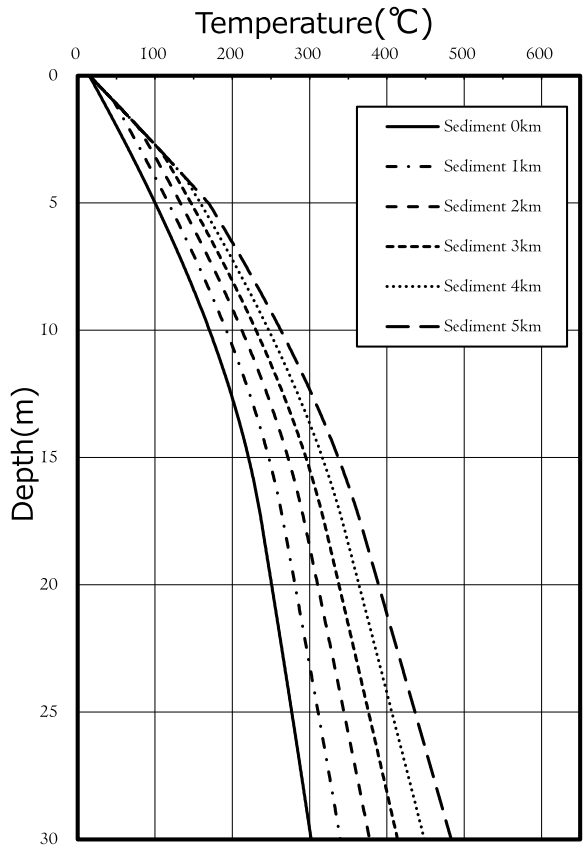

Fig. 11 Example of underground temperature calculation (2). An example calculation shows the effect of a sedimentary layer. The heat flow is 50 mW m^{-2}. The crustal structure corresponds to Model A (Case A-5) in Fig. 9(a)

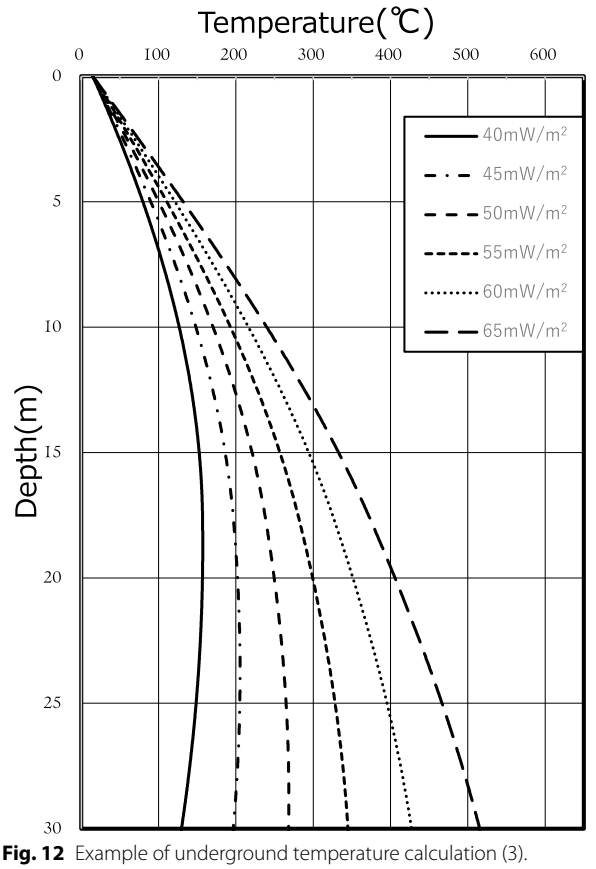

Fig. 12 Example of underground temperature calculation (3). Example calculation for Model B (Case B-1) with low heat flow. There are six cases with heat flow of 40 mW m^{-2}, 45 mW m^{-2}, 50 mW m^{-2}, 55 mW m^{-2}, 60 mW m^{-2}, and 65 mW m^{-2}

the lower crustal mafic rocks is 800 °C, and the temperature of the Moho discontinuity (30 km depth) is 900 °C. If the temperature reached 650 °C in the upper crust, the model was designed to monotonically increase over depth to reach 900 °C at a Moho discontinuity depth of 30 km. If the temperature did not reach 650 °C in the upper crust but reached 800 °C in the lower crust, the temperature was assumed to increase to reach 900 °C at a depth of the Moho discontinuity monotonically.

Result

The subsurface temperature was calculated for 126 Hi-net borehole wells, 86 DTPBJ wells, and 1 MITI exploratory test well for 213 locations. Figure 13 shows the temperature distribution at depths of 5 km, 10 km, 15 km, and 20 km, and Fig. 14 shows the depth of the 300 ℃, 400 ℃, and 450 ℃ isotherm, based on Model A and Model B. The depth distribution of isotherms for Model C is shown in Fig. 15. Depths are converted to depths from 0 m above sea level, not surface. Nearest

(See figure on next page.)

Fig. 13 Map of estimated subsurface temperatures. Estimated temperatures at depths of 5 km (**a**), 10 km (**b**), 15 km (**c**), and 20 km (**d**) are shown. The subsurface temperatures obtained at each measurement point are interpolated by averaging filtering based on the nearest neighbor method. The grid size was set to 4 min, and the search area to 50 km. Based on the values of this grid, isotherms were described at 100 °C intervals. Note that since a simplified method is used to estimate the solidus temperature above 650 °C, the values in the high-temperature region have relatively large uncertainties at 15 km (**c**) and 20 km (**d**)

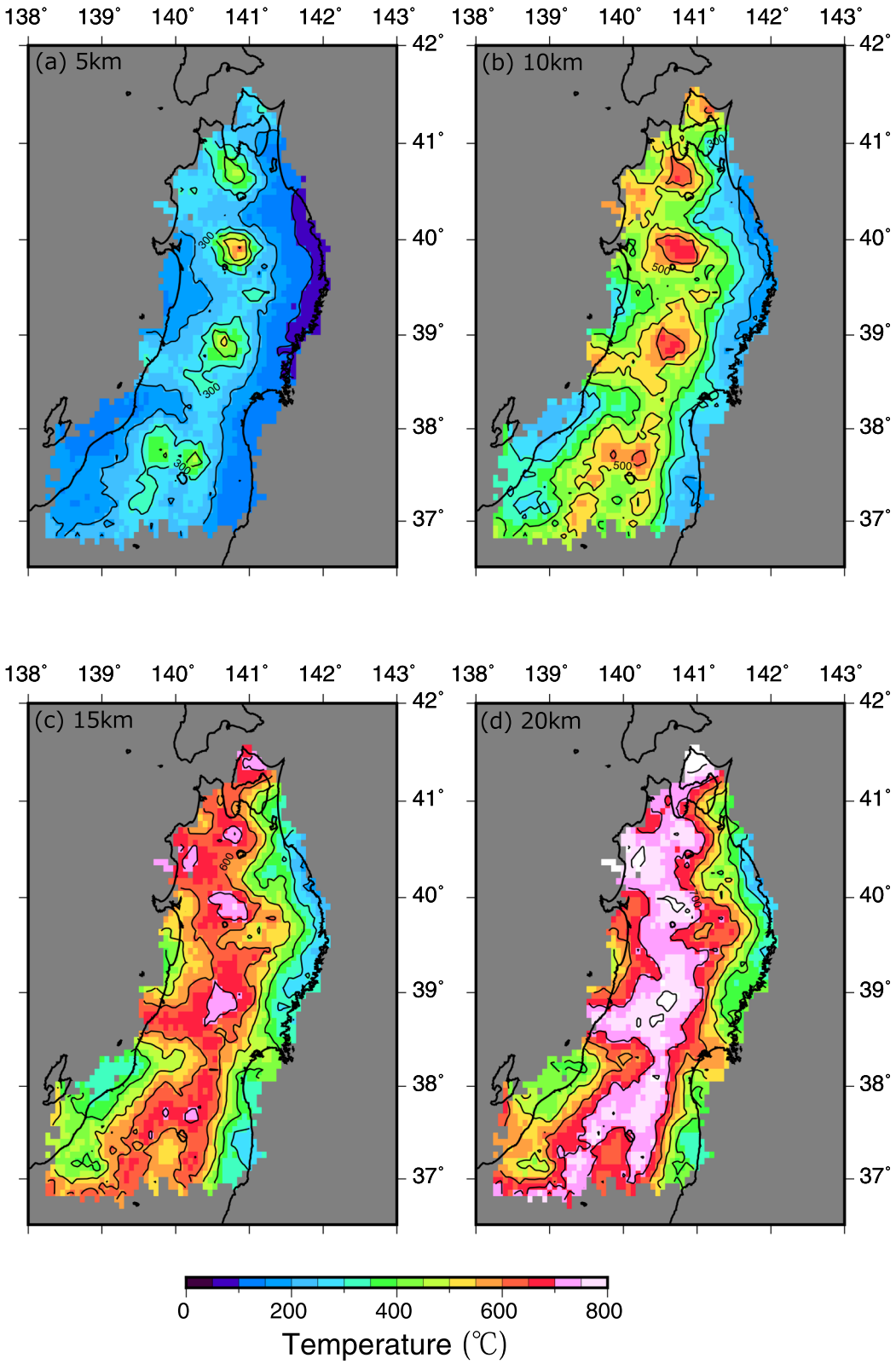

Fig. 13 (See legend on previous page.)

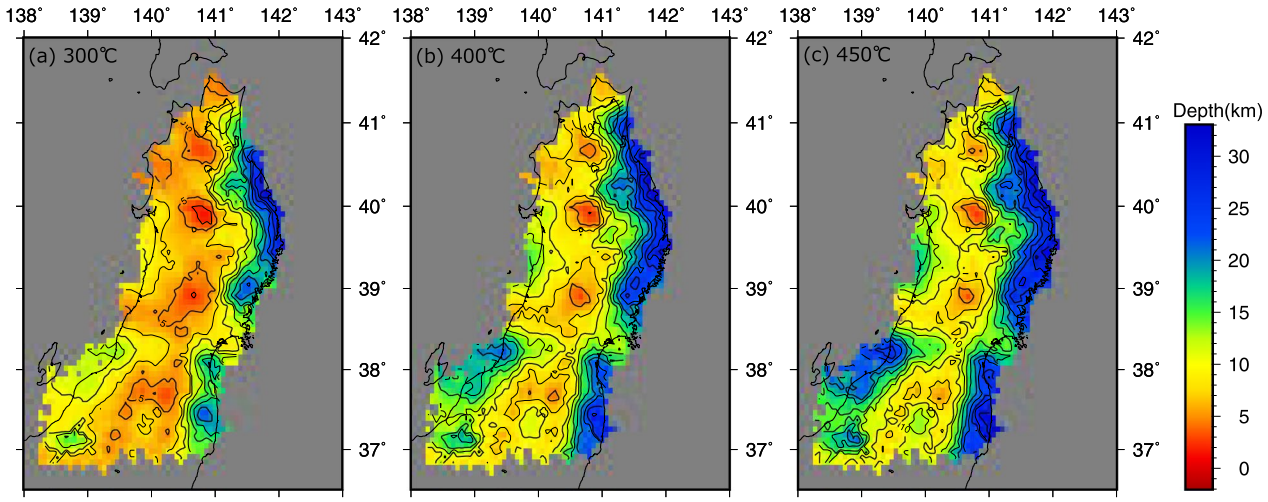

Fig. 14 The depth of the 300 ℃, 400 ℃, and 450 ℃ (Model A + B). This study estimated depth profiles of 300 °C, 400 °C, and 450 °C (Model A + B). The depth values reaching each temperature obtained at each measurement point are interpolated by averaging filtering based on the nearest neighbor method. The grid size was set to 4 min, and the search area to 50 km. Based on the values of this grid, isobaths were described at 2.5 km intervals

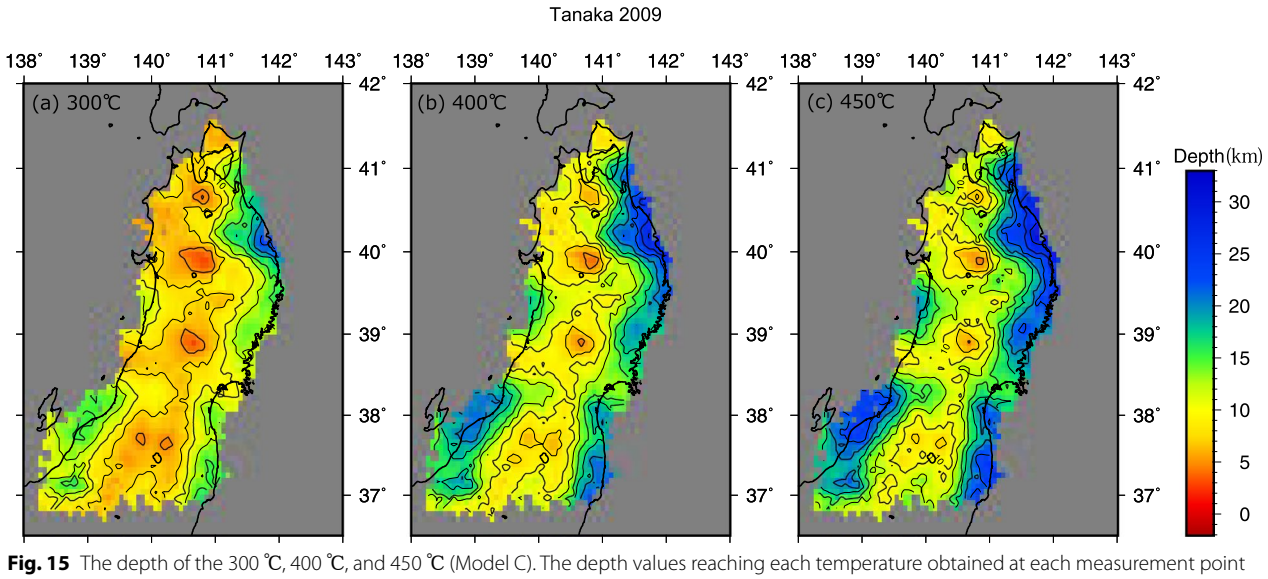

Fig. 15 The depth of the 300 ℃, 400 ℃, and 450 ℃ (Model C). The depth values reaching each temperature obtained at each measurement point are interpolated by averaging filtering based on the nearest neighbor method. The grid size was set to 4 min, and the search area to 50 km. Based on the values of this grid, isobaths were described at 2.5 km intervals

neighbor interpolation was used to create the map. The interpolated grid size was set to 4 min or approximately 7.5 km, and a filter was used to interpolate from the values of multiple observation points within a 50-km radius. Isotherms were created in 100 °C steps based on the values for each grid.

The high-temperature region extends along the central axis of the Ou Backbone Range, and local high-temperature anomalies exist around volcanoes distributed along this axis. Therefore, there are many places where the depth of 650 °C is less than 10 km in these regions. On the other hand, in the coastal area on the forearc side,

where low heat flow regions of about 50 mW m^{-2} exist, a low-temperature structure of about 300 °C to 400 °C is estimated at a depth of 30 km. In the low heat flow region in the southern part of the back-arc, where the thickness of the sedimentary layer is as much as 5 km, the temperature structure is about 300 °C at a depth of 10 km.

Discussion

Heat flow

Heat flow distribution and characteristics

Compared with the previous study by Tanaka et al. (2004), shown in Fig. 8b, and Sakagawa et al. (2006), shown in Fig. 8c, the spatial distribution of heat flow characteristics shows almost the same trend. Compared to the geothermal gradient distribution shown in Fig. 8a (Tanaka et al. (2004)), the same trend appears to be true. By interpolating the forearc side, where the amount of data was previously small, it can be said that entire Northeastern Japan can now be covered, although the amount of data for the plains in the northern region is relatively small. Along the Ou Backbone Range, where the present volcanic front (VF) is located, many heat flow data estimates above 200 mW m^{-2}. On the forearc side, heat flow is generally low in the area, but some heat flow data are estimated to be around 100 mW m^{-2} in some parts of the area. In addition, many heat flow data exceeding 200 mW m^{-2} have been estimated along the Ou Backbone Range.

On the other hand, low heat flow areas can extend to the plains and other areas. Low heat flow areas are distributed on the forearc side, especially in the northern and southern parts of the Kitakami Mountains, the eastern part of the Abukuma Mountains, and near the Niigata Plain on the back-arc side.

Influence of subsurface fluids

Tamanyu (2008) proposed a model of hydrothermal convection related to the thickness of the sedimentary layers in Northeastern Japan and estimated that hydrothermal convection is dominant down to the depth of the Pre-Paleogene basement rocks, from 1 to 3 km in plains and basins, and up to 1 km in volcanic regions. For example, hydrothermal convection systems are thought to be dominant in areas where high heat flow is observed, which exist around volcanoes in the Ou Backbone Range. In this case, the near-surface heat flow is the heat transfer due to heat conduction at depth plus the heat transfer due to fluid at shallow depth.

Therefore, overestimated heat flow values may be used when estimating the temperature structure at depths greater than a few kilometers. Sakagawa et al. (2006), who have conducted many heat flow analyses, especially in geothermal regions, analyzed heat flow due to heat conduction and heat flow due to fluid involvement in many borehole wells and estimated that heat as much as the heat conduction flux is transported to the surface by fluids. Therefore, it should be noted that estimating the temperature structure of the subsurface in areas that exhibit such high heat flow is subject to fluid effects.

On the other hand, it has been pointed out that groundwater flow systems are widespread in the plains (Miyakoshi and Uchida 2001). In these areas, subsurface temperature gradients are complex, with large temperature gradients in the ascending groundwater basins and small temperature gradients in the descending basins (Uchida et al. 2014; Kaneko et al. 2020). On the other hand, most of the D-class wells, which were judged to have powerful groundwater influence, are in the plains with thick sedimentary layers, and their temperature profiles show downward flow type. The temperature profiles of the Hi-net borings showed the influence of surface groundwater in about 10% of the stations, including the C-class wells that were judged to be partially affected. Heat flow in these boreholes is generally estimated to be low. Therefore, more careful analysis that considers groundwater effects may be necessary, especially for borehole wells in geological conditions such as basins and plains where sedimentary layers are thick, and water can easily penetrate.

High heat flow regions and volcanic distribution

In geothermal zones in plains with thick sedimentary layers and around volcanoes, shallow ground structures and groundwater behavior are thought to influence heat flow strongly, and we attempt to interpret the heat flow distribution obtained in this study based on the assumption of the existence of these effects. First, we attempt here to discuss the distribution of high heat flow regions. It is said that in subduction zones, low heat flow is observed on the forearc side, high heat flow on the VF, and moderate heat flow on the back-arc side (e.g., Fukahata and Matsu'ura 2000), and we first examine regions where this pattern and high heat flow distribution are different. Then, we find that there is a region of high heat flow along the eastern side of the Ou Backbone Range.

In the central part of the Kitakami Mountains and near the Sendai Plain, there are areas of high heat flow extending from the VF to the forearc side. Therefore, we will consider the current distribution of volcanoes and the correlation with the past distribution of volcanoes. The position of the VF in Northeastern Japan was about 30–40 km east of its present position at 16 Ma, but it has moved from about 10 km west to east at 10 Ma (Yoshida et al. 2013). Consider the possibility that these past VF movements still influence the thermal structure of the

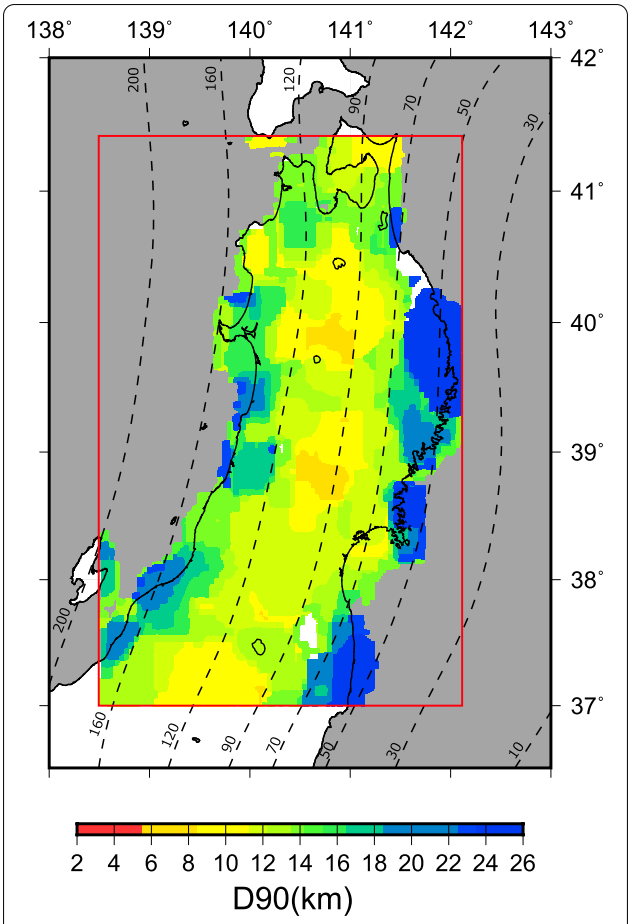

Fig. 16 The spatial distribution of D90, the cut-off depth of shallow seismicity in Northeastern Japan. D90 is the depth above which 90% of the earthquakes occur. The D90 distribution for the area enclosed by the red line is based on Omuralieva et al, (2012). The dotted lines denote depth (km) contours to the top of the subducted Pacific plate (PAC) slab (Iwasaki et al. 2015; Lindquist et al. 2004)

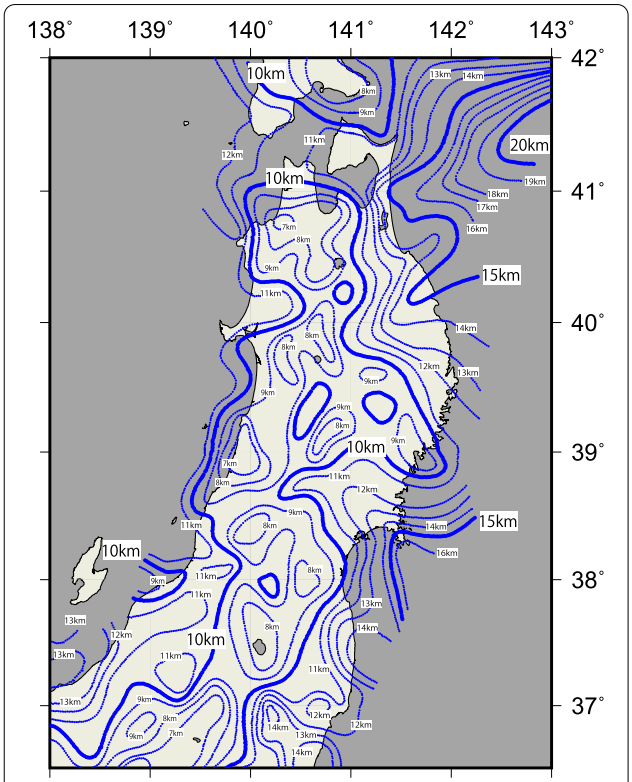

Fig. 17 Curie depth contour map of Northeastern Japan, indicating the locations of temperature measurements. Curie depth contour interval is 1 km, the contours denoting inferred Curie depths (km) below sea level. Based on Okubo et al. (1989)

crust. Since 8 Ma, many large calderas have formed along the central axis of the Ou Backbone Range (Yoshida et al. 2013), but only one caldera has been identified on the forearc side of the present VF.

The time required to cool a magma reservoir with a diameter of 10 km is said to be about 1 Ma (Tomiya 2000), so the time scales may not match. On the other hand, there are cases where calderas are assumed to have been active for more than 600,000 years after their formation (Takehara et al. 2017), and hydrothermal reservoirs and low-velocity bodies have been observed beneath calderas formed in the Late Miocene (Sato et al. 2002). It has also been pointed out that magma reservoirs with lifetimes longer than several million years may exist if conditions like continuous fluid supply from deep underground are met (Yoshida et al. 2020). However, the distribution of calderas in Northeastern Japan (Yoshida et al. 2013) shows no evidence of calderas extending over the central Kitakami Mountains and the Sendai Plain. Therefore, the cause of this high heat flow is unrelated to the VF, and we should consider that other factors bring about the high heat flow.

Low heat flow regions

Next, we will discuss the distribution of the low heat flow regime. As discussed in the previous section, we will focus on the differences from the assumed pattern of heat flow distribution in the subduction zone. For example, in the northern part of the Kitakami Mountains, areas of low heat flow are on the Ou backbone Range side of the VF. As mentioned in the previous subsection, the VF existed about 30–40 km east of the present at 16 Ma (Yoshida et al. 2013), but the time when the VF existed west of the present, where low heat flow is expected, goes back to 30 Ma, and it is estimated that it existed near the present Japan Sea coastline at that time (Sato 1994). Therefore, the relationship between the movement of the VF and the existence of a region of low heat flow near the

northern Kitakami Mountains, which extend farther to the Ou Backbone Range than the VF, is unclear.

Although heat flow is low in areas where crustal subsidence and sedimentation are in progress (e.g., Fukahata and Matsu'ura 2000), the cause of this is also unknown because the area is not significantly subsided compared to the analysis of crustal deformation in Northeastern Japan over the past 120 years (Nishimura 2012). On the other hand, the Niigata Plain on the back-arc side also has many areas of low heat flow, but these are areas where sedimentation is estimated to be high (Nishimura 2012; Kobayashi 1996), and in these areas, the consistency between low heat flow and crustal activity is recognized to some extent. The impact of this crustal movement and the current tectonic setting that drives it on the distribution of heat flow will need to be examined, including the results of estimating the subsurface thermal structure.

Thermal structure

D90 and thermal structure

In order to examine the validity of the calculated temperature structure, we first compare it with the D90 distribution estimated by Omuralieva et al. (2012), shown in Fig. 16, which is an indicator of the lower limit of the seismogenic layer of the crust. There seems to be a good correlation between the temperature structure and the spatial distribution of D90, and the isotherm at a depth of 400 °C and 450 °C is correlated. On the other hand, in the case of Model C (Fig. 15), where isobaths were calculated for comparison, the correlation seems to be at 400 °C or slightly cooler.

Further study of the correlation between Model A + B and D90: among 300 °C, 400 °C, and 450 °C, the 450 °C isothermal depth and the D90 depth seems to be consistent overall. Along the Ou Backbone Range, both isothermal depth and D90 are shallow, but the isothermal depth is slightly different where it is estimated to be shallower. On the forearc side, isothermal depths tend to be consistent in the south near the Kitakami Mountains but slightly different in the north, where isothermal depths tend to be deeper than those of D90. Finally, in the Sendai Plain area, where the D90 is shallower, the isothermal depth is consistent with 450 °C or 400 °C (Fig. 16).

Next, the back-arc side is examined. The Niigata Plain, the epicenter of the Mid Niigata Prefecture Earthquake in 2004, is an area with thick sedimentary layers (Kobayashi 1996). There is a good correlation between temperature and the lower limit of the seismogenic layer in this area, which shows the effect of introducing a detailed crustal structure. On the back-arc side, isothermal depth is consistent with 450 °C near the Niigata Plain, but D90 tends to be a little deeper in areas farther north.

Thus, while regional differences between D90 and the inferred temperature structure may be seen, the relationship between the lower limit of the seismogenic zone and the depth to the brittle–ductile transition in the crust has been extensively investigated in seismically active lithotectonic belts (e.g., Magistrale and Zhou (1996); Albaric et al. 2009; Hauksson and Meier 2019). In addition, some reports suggest that the occurrence of shallow intraplate earthquakes is governed by friction that depends on the temperature and lithology of the upper crust (Maeda et al. 2021). The characteristics of the subsurface temperature structure obtained in this study may provide information on how D90 temperatures vary with depth, lithology, and other factors.

Curie point depth and thermal structure

Next, we compare it with the Curie point temperature distribution by Okubo et al. (1989), shown in Fig. 17. Although both have resolution limitations, there seems to be a good correlation in terms of trends in spatial distribution. However, compared to the estimated temperatures, Model A + Model B (Fig. 14) seems to match 400 °C near the Ou Backbone Range and 300 °C on the back-arc and forearc sides. As mentioned in the previous section, there is a region of low heat flow extending from the northern side of the Kitakami Mountains to the Ou Backbone Range side of the VF, and there is a correlation between this distribution and the Curie point temperature distribution. However, there is no clear correlation between the distribution of high heat flow in the central part of the Kitakami Mountains and the Sendai Plain.

This Curie point temperature distribution is interpreted by Nishida and Hashimoto (2007) as corresponding to 400–450 °C, or about 300 °C, depending on the rock type. However, as with D90, this may need to be carefully considered in terms of the physical conditions of the rock.

Influence of tectonic models

Now that we have mentioned that the rock zone's physical conditions (temperature, structure, and lithology) are essential issues, we will again review the tectonic model of this study. First, the crustal structure is assumed to be a simple horizontal layered structure with an upper crustal thickness of 18 km and a lower crustal thickness of 12 km. However, in many models, the Moho discontinuity is estimated to be deeper just below the Ou Backbone Range and slightly shallower on the frontal and back-arc sides (e.g., Nishimoto et al. 2005; Muto and Ohzono 2012; Matsubara et al. 2017a).

Since the thickness of the upper crust determines the total amount of crustal heat generation, heterogeneity in the upper crust's thickness significantly impacts the lower crust's estimated temperature structure. In addition, the 3D seismic velocity structure shows heterogeneity (e.g., Matsubara et al. 2017b), making it likely that the crustal components are not simple horizontal layers. The model used in this study is that the lower crust near the Kitakami Mountains is composed of granite (Nishimoto et al. 2008; Ishikawa et al. 2014; Ishikawa, 2017). Since the thermal conductivity and amount of radiative heat generation vary depending on the type of rock, it will be necessary to construct a 3-D structure that considers these characteristics. The existence of high heat-flow regions on the forearc side and low heat-flow regions near the VF may be explained to some extent by the heterogeneity of heat generation in the upper and lower crust.

In addition, Northeastern Japan is an area where tectonic inversion is in progress (Sato 1994), and as Fukahata and Matsu'ura (2000) point out, the influence of the active crustal movement of uplifts such as uplifts and sedimentation needs to be taken into account.

However, this method, which considers the detailed structure of the crust, tends to estimate temperatures on the low side for low heat fluxes and on the high side for high fluxes, compared to previous studies. A further improvement of this method would be to consider heat transfer by fluids. For a more accurate estimation, it may be helpful to use an approach proposed by Sakagawa et al. (2006) to elaborately model the heat flux, which is the sum of heat conduction in the rock mass and heat transport by the fluid, as observed heat flow at the surface. In the future, it will be necessary to collaborate with groundwater models, for example, to separate the heat flux from the surface to 1 to 2 km, where the influence of fluid is significant, from the heat conduction below the base rock conduction is dominant.

For example, a factor other than structure is the behavior of fluids deep in the crust. Nakajima and Hasegawa (2003) proposed a model in which an S-wave reflection surface exists on the east side of the volcanic front, and water is supplied from the lower crust. The effect on the thermal structure of the movement of such fluids from the lower crust to the upper crust, such as the cause of the high heat-flow regions that exist east of the VF and on the forearc side, would need to be considered.

Mantle wedge

Finally, the relationship between deep structure and temperature structure, i.e., the possibility that the temperature structure of the mantle wedge may affect the inferred thermal structure, is discussed. Compared to the hot finger model (Tamura et al. 2002), in which particularly hot regions of the mantle wedge are distributed at regular intervals, the spatial distribution of regions hotter than the surroundings appears to be in good agreement. However, a quantitative comparison may be difficult since this study uses a simplified model for calculating thermal structure above the solidus temperature.

The lower temperatures, especially on the forearc side, may also be consistent with the model inferred by Wada and Wang (2009) and Wada et al. (2011) that the slab and the mantle are fully decoupled until a depth of 70–80 km, but fully coupled at greater depths. Using shear-wave splitting analysis, Uchida et al. (2020) found a distinct lack of anisotropy in the forearc mantle wedge, indicating that the forearc mantle wedge is decoupled from the slab and does not participate in the viscous flow. While the correlation between the location of the 70-km slab isobath (Fig. 16) and the low-temperature regions in the estimated temperature distribution (Fig. 14) is certainly good, the low-temperature regions in the northern Kitakami Mountains and the high-temperature regions in the central Kitakami Mountains may become consistent if we assume some regional variation in the depth at which these mantle wedges become uncoupled to the slab, for example.

Suppose these issues can be overcome, such as addressing the behavior of groundwater in the shallow part of the crustal structure model used to estimate thermal structure in this study and the behavior of fluids rising from deeper parts of the crust. In that case, it may be possible to increase the accuracy required for comparison with D90 and improve the accuracy of temperature estimates to the Moho discontinuity.

Conclusion

New heat flow data covering Northeastern Japan, corrected for climate change, were obtained using borehole temperature profiles of the NIED Hi-net. The obtained spatial distribution of heat flow shows low heat flow on the forearc side, high heat flow along the Ou Backbone Range, and low heat flow in the plains on the back-arc side. However, the distribution is not clearly divided into high and low heat flow along the VF front; for example, the low heat flow extends from near the northern Kitakami Mountains on the forearc side to the Ou Backbone Range crossing the VF, while the high heat flow extends to the central Kitakami Mountains and Sendai plain on the forearc side. In addition, the crustal temperature structure was obtained by using a crustal structure model that takes into account the temperature dependence of thermal conductivity and the difference in heat generation due to lithology, using a crustal structure model that takes into account sedimentary

layers rather than a uniform structure model with exposed bedrock at the surface.

Good correlation was observed with D90 and Curie point depth distribution, with D90 ranging from 400 to 450 °C, Curie point depth around 400 °C near the Ou Backbone Range, and a strong correlation around 300 °C on the anterior and back-arc sides. Compared to previous studies, the crustal thermal structure calculation method assumed is a model whose estimated temperature distribution is sensitive to structural differences; however, a more accurate estimation of the temperature structure is possible if detailed structural information is available.

On the other hand, it seems necessary to treat fluid behavior in more detail in areas of high heat flow. However, the estimation of crustal temperature structure, especially in regions with thick sedimentary layers, is considered an improvement over the previous study. We hope that this study will be useful in developing initial models for future complex analyses of crustal thermal structure.

Acknowledgements
The comments from two anonymous reviewers were very helpful in revising the manuscript. The authors are very grateful to Keiji Kasahara, Kazushige Obara, Katsuhiko Shiomi, Youichi Asano, Akira Yamamoto, and Kentaro Omura for their support of this work. Some figures were drawn using the Generic Mapping Tools software package (Wessel and Smith 1998). The plate models by Iwasaki et al. (2015) were constructed from topography and bathymetry data by the Geospatial Information Authority of Japan (250-m digital map), Japan Oceanographic Data Center (500 m mesh bathymetry data, J-EGG500, http://www.jodc.go.jp/jodcweb/JDOSS/infoJEGG_j.html) and Geographic Information Network of Alaska, University of Alaska (Lindquist et al. 2004).

Author contributions
TM conducted the data analysis and prepared the manuscript. RY measured heat flow data and participated in the design of the discussion. SI participated in the design of the discussion. All of the authors read and approved the final manuscript.

Funding
Not applicable.

Availability of data and materials
The datasets used and/or analyzed during the current study are available from the corresponding author on reasonable request.

Declarations

Ethics approval and consent to participate
Not applicable.

Consent for publication
Not applicable.

Competing interests
The authors declare that they have no competing interests.

Received: 8 January 2022 Accepted: 3 September 2022
Published online: 19 October 2022

References

Akiyama M, Hirai A (1997) Maximum paleotemperature gradient using vitrinite reflectance mainly of the government MITI exploratory test wells. J Jpn Assoc Petrol Technol 62(1):69–79. https://doi.org/10.3720/japt.62.69 (**in Japanese with English abstract**)

Albaric J, Déverchère J, Petit C, Perrot J, Le Gall B (2009) Crustal rheology and depth distribution of earthquakes: insights from the central and southern East African Rift System. Tectonophysics 468(1–4):28–41. https://doi.org/10.1016/j.tecto.2008.05.021

Aoi S, Asano Y, Kunugi T, Kimura T, Uehira K, Takahashi N, Ueda H, Shiomi K, Matsumoto T, Fujiwara H (2020) MOWLAS: NIED observation network for earthquake, tsunami and volcano. Earth Planets Space 72:126. https://doi.org/10.1186/s40623-020-01250-x

Arakawa Y, Shinohara A (1981) Rapid measurement of thermal conductivity. Oyo Buturi 50(6):661–666. https://doi.org/10.11470/oubutsu1932.50.661 (**in Japanese**)

Beardsmore GR, Cull CP (2001) Crustal heat flow: a guide to measurement and modeling. Cambridge Univ. Press, Cambridge

Bodri B, Iizuka S, Hayakawa M (1989) Modeling of deep temperature and heat flow in central Honshu, Japan. J Geodynamics 11:105–129. https://doi.org/10.1016/0264-3707(89)90011-2

Cermak V, Rybach L (1982) Thermal properties. In: Angenheister G (ed) Physical properties of rocks. Springer, New York, pp 305–481

Dakin JP, Pratt DJ, Bibby GW, Ross JN (1985) Distributed optical fiber Raman temperature sensor using a semiconductor light source and detector. Electron Lett 21:569–570. https://doi.org/10.1049/el:19850402

Erkan K (2015) Geothermal investigations in western Anatolia using equilibrium temperatures from shallow boreholes. Solid Earth 6:103–113. https://doi.org/10.5194/se-6-103-2015

Erkan K, Blackwell DD (2008) A thermal test of the post-subduction tectonic evolution along the California transform margin. Geophys Res Lett 35:L07309. https://doi.org/10.1029/2008GL033479

Fujibe F (2012) Evaluation of background and urban warming trends based on centennial temperature data. Pap Meteor Geophys 63:43–56. https://doi.org/10.2467/mripapers.63.43

Fukahata Y, Matsu'ura M (2000) Effects of active crustal movements on thermal structure in subduction zones. Geophys J Int 141:271–281. https://doi.org/10.1046/j.1365-246x.2000.00120.x

Funnell R, Chapman D, Allis R, Armstrong P (1996) Thermal state of the Taranaki Basin, New Zealand. J Geophys Res 101:25197–25215. https://doi.org/10.1029/96JB01341

Furukawa Y, Uyeda S (1986) Thermal state under tohoku arc with consideration of crustal heat generation. Bull Volcanol Soc Jpn 31(1):15–28. https://doi.org/10.18940/kazanc.31.1_15 (**in Japanese with English abstract**)

Gueguen Y, Palciauskas V (1994) Introduction to the physics of rocks. Princeton University Press, Princeton

Hauksson E, Meier MA (2019) Applying depth distribution of seismicity to determine thermo-mechanical properties of the seismogenic crust in Southern California: comparing lithotectonic blocks. Pure Appl Geophys 176(3):1061–1081. https://doi.org/10.1007/s00024-018-1981-z

Ikebe Y, Ozawa A, Inoue H (1979) Geology of the GOSHOGAWARA district. Quadrangle series scale1: 50,000 Akita 6(55). https://www.gsj.jp/data/50KGM/PDF/GSJ_MAP_G050_06055_1979_D.pdf (**in Japanese with English abstract**)

Ishikawa M (2017) Deep crustal and uppermost mantle lithology of Island Arcs: Izu Arc and NE Honshu Arc. J Geol Soc Jpn 123(6):355–364. https://doi.org/10.5575/geosoc.2017.0027 (**in Japanese with English abstract**)

Ishikawa M, Matsubara M, Takeda T (2014) Felsic lower crust and orthopyroxenitic mantle beneath the Kitakami Mountains, Japan: evidence for slab melting in the Cretaceous. Jpn Mag Mineral Petrol Sci 43(3):100–107. https://doi.org/10.2465/gkk.140120 (**in Japanese with English abstract**)

Ito A, Fujie G, Tsuru T, Kodaira S, Nakanishi A, Kaneda Y (2004) Fault plate geometry in the source region of the 1994 Sanriku-oki earthquake. Earth Planet Sci Lett 223:16. https://doi.org/10.1016/j.epsl.2004.04.007

Ito Y, Tsuji T, Osada Y, Kido M, Inazu D, Hayashi Y, Tsushima H, Hino R, Fujimoto H (2011) Frontal wedge deformation near the source region of the 2011 Tohoku-Oki earthquake. Geophys Res Lett 38:L00G05. https://doi.org/10.1029/2011GL048355

Iwasaki T, Kato W, Moriya T, Hasemi A, Umino N, Okada T, Miyashita K, Mizogami T, Takeda T, Sekine S, Matsushima T, Tashiro K, Miyamachi H (2001) Extensional structure in Northern Honshu Arc as inferred from seismic refraction/wide-angle reflection profiling. Geophys Res Lett 28:2329–2332. https://doi.org/10.1029/2000GL012783

Iwasaki T, Sato H, Shinohara M, Ishiyama T, Hashima A (2015) Fundamental structure model of island arcs and subducted plates in and around Japan. 2015 Fall Meeting, AGU, San Francisco, California, 14–18 Dec 2015. Abstract T31B–2878.

Jessop AM (1990) Thermal geophysics. Elsevier, Amsterdam, p 306

JMA (2016) Climate Change in Tohoku. JMA https://www.data.jma.go.jp/sendai/knowledge/climate/change/report.html (**in Japanese**)

JMA (2022) A mean annual temperature in Japan https://www.data.jma.go.jp/cpdinfo/temp/an_jpn.html(**in Japanese**)

Kaneko S, Tomigashi A, Ishihara T, Shrestha G, Yoshioka M, Uchida Y (2020) Proposal for a method predicting suitable areas for installation of ground-source heat pump systems based on response surface methodology. Energies 13(8):1872. https://doi.org/10.3390/en13081872

Kobayashi I (1996) Quaternary Geology of the Echigo Plain, Niigata, Japan. Quat Res (daiyonki-Kenkyu) 35(3):191–205. https://doi.org/10.4116/jaqua.35.191

Lindquist KG, Engle K, Stahlke D, Price E (2004) Global topography and bathymetry grid improves research efforts. Eos Trans AGU 85(19):186. https://doi.org/10.1029/2004EO190003/abstract

Maeda S, Toda S, Matsuzawa T, Otsubo M, Matsumoto T (2021) Influence of crustal lithology and the thermal state on microseismicity in the Wakayama region, southern Honshu. Jpn Earth Planets Space 73:173. https://doi.org/10.1186/s40623-021-01503-3

Magistrale H, Zhou HW (1996) Lithologic control of the depth of earthquakes in Southern California. Science 273(5275):639–642. https://doi.org/10.1126/science.273.5275.639

Matsubara M, Sato H, Ishiyama T, Van Horne AD (2017a) Configuration of the Moho discontinuity beneath the Japanese Islands derived from three-dimensional seismic tomography. Tectonophysics 710–711:97–107. https://doi.org/10.1016/j.tecto.2016.11.025

Matsubara M, Sato H, Uehira K, Mochizuki M, Kanazawa T (2017b) Three-dimensional seismic velocity structure beneath Japanese islands and surroundings based on NIED seismic networks using both inland and offshore events. J Disaster Res 12(5):844–857. https://doi.org/10.20965/jdr.2017.p0844

Matsumoto T (2007) Terrestrial heat flow distribution in Japan area based on the temperature logging in the borehole of NIED Hi-net. 2007 Fall Meeting, AGU, San Francisco, California, 10–14 Dec 2007. Abstract T23A-1217.

Miao SQ, Li HP, Chen G (2014) Temperature dependence of thermal diffusivity, specific heat capacity, and thermal conductivity for several types of rocks. J Therm Anal Calorim 115:1057–1063. https://doi.org/10.1007/s10973-013-3427-2

Minato S (2005) Uranium, thorium and potassium concentrations in Japanese soils. Radioisotopes 54:509–515. https://doi.org/10.3769/radioisotopes.54.509

Miyakoshi A, Uchida Y (2001) Distribution of subsurface temperature and groundwater flow system in the Kanto Plain. Bull Geol Surv Japan 52(6):253–290. https://doi.org/10.9795/bullgsj.52.253 (**in Japanese with English abstract**)

Muto J, Ohzono M (2012) Rheological profile across the northeastern Japan lithosphere toward precise modeling of the 2011 Tohoku Oki Earthquake. Jour Geol Soc Japan 118:323–333. https://doi.org/10.5575/geosoc.2012.0026 (**in Japanese with English abstract**)

Muto J, Shibazaki B, Ito Y, Iinuma T, Ohzono M, Matsumoto T, Okada T (2013) Two-dimensional viscosity structure of the northeastern Japan islands arc-trench system. Geophys Res Lett 40:4604–4608. https://doi.org/10.1002/grl.50906

Nakajima J, Hasegawa A (2003) Tomographic imaging of seismic velocity structure in and around the Onikobe volcanic area, northeastern Japan: implications for fluid distribution. J Volcanol Geotherm Res 127:1–18

National Research Institute for Earth Science and Disaster Resilience (2019) J-SHIS, National Research Institute for Earth Science and Disaster Resilience. https://doi.org/10.17598/nied.0012

Nishida Y, Hashimoto T (2007) Geothermal structure of the crust and the upper mantle in Hokkaido, Japan: a review. Geophys Bull Hokkaido Univ 70:1–12. https://doi.org/10.14943/gbhu.70.1 (**in Japanese with English abstract**)

Nishimoto S, Ishikawa M, Arima M, Yoshida T (2005) Laboratory measurement of P wave velocity in crustal and upper mantle xenoliths from Ichino-megata, NE Japan: ultrabasic hydrous lower crust beneath the NE Honshu arc. Tectonophysics 396:245–259. https://doi.org/10.1016/j.tecto.2004.12.010

Nishimoto S, Ishikawa M, Arima M, Yoshida T, Nakajima J (2008) Simultaneous high P–T measurements of ultrasonic compressional and shear wave velocities in Ichino-megata mafic xenoliths: Their bearings on seismic velocity perturbations in lower crust of northeast Japan arc. J Geophys Res 113:B12212. https://doi.org/10.1029/2008JB005587

Nishimura T (2012) Crustal deformation of northeastern Japan based on geodetic data for recent 120 years. J Geol Soc Jpn 118(5):278–293. https://doi.org/10.5575/geosoc.2012.0027 (**in Japanese with English abstract**)

Nishisaka H, Shinohara M, Sato T, Hino R, Mochizuki K, Kasahara J (2001) Crustal structure of the Yamato basin and the margin of the north- eastern Japan Sea using ocean bottom seismographs and controlled sources. Zisin 54(3):365–379. https://doi.org/10.4294/zisin1948.54.3_365 (**in Japanese with English abstract**)

Okada Y, Kasahara K, Hori S, Obara K, Sekiguchi S, Fujiwara H, Yamamoto A (2004) Recent progress of seismic observation networks in Japan -Hi-net, F-net, K-NET and KiK-net. Earth Planets Space 56:15–28. https://doi.org/10.1186/BF03353076

Okubo Y, Tsu H, Ogawa K (1989) Estimation of Curie point temperature and geothermal structure of island arcs of Japan. Tectonophysics 159:279–290. https://doi.org/10.1016/0040-1951(89)90134-0

Okubo Y, Akita F, Tanaka A (1998) Thermal gradient map and thermal structural model—a case study of Hokkaido. J Geotherm Res Soc Japan 20(1):15–29. https://doi.org/10.11367/grsj1979.20.15 (**in Japanese with English abstract**)

Omuralieva AM, Hasegawa A, Matsuzawa T, Nakajima J, Okada T (2012) Lateral variation of the cutoff depth of shallow earthquakes beneath the Japan Islands and its implications for seismogenesis. Tectonophysics 518–521:93–105. https://doi.org/10.1016/j.tecto.2011.11.013

Ozawa A, Hirayama J (1970) Geology of the GOSHOGAWARA district. Quadrangle series scale1: 50,000 Aomori 5(21) https://www.gsj.jp/data/50KGM/PDF/GSJ_MAP_G050_05021_1970_D.pdf (**in Japanese with English abstract**)

Pollitz F (1986) Pliocene change in Pacific plate motion. Nature 320:738–741. https://doi.org/10.1038/320738a0

Robertson JK, Wyllie PJ (1971) Rock-water system, with special reference to the water-deficient region. Amer J Sci 271:252–277. https://doi.org/10.2475/ajs.271.3.252

Royer JJ, Danis M (1988) Steady state geothermal model of crust and the problem of the boundary conditions: application to a rift system, the southern Rhinegraben. Tectonophysics 156:239–255. https://doi.org/10.1016/0040-1951(88)90062-5

Sakagawa Y, Umeda K, Suzuki M, Kajiwara T, Uchida Y (2004) Database on the Temperature Profiles of Boreholes in Japan. Zisin 57:63–67. https://doi.org/10.4294/zisin1948.57.1_63 (**in Japanese**)

Sakagawa Y, Umeda K, Asamori K (2006) Heat flux distribution in Japan taking account of advection processes. J Geotherm Res Soc Jpn 28(2):211–221. https://doi.org/10.11367/grsj1979.28.211 (**in Japanese with English abstract**)

Sato H (1994) The relationship between late Cenozoic tectonic events and stress field and basin development in northeast Japan. J Geophys Res 99:22261–22274. https://doi.org/10.1029/94JB00854

Sato H, Imaizumi T, Yoshida T, Ito H, Hasegawa A (2002) Tectonic evolution and deep to shallow geometry of Nagamachi-Rifu Active Fault System, NE Japan. Earth Planets Space 54:1039–1043. https://doi.org/10.1186/BF03353298

Sato T, Taniguchi W, Fujita T, Hasegawa H (1999) Data Collection by Literature Survey on Rock Physical Properties in Japan (II), JNC TN7400 99–011, Japan Nuclear Cycle Development Institute (**in Japanese with English abstract**). https://jopss.jaea.go.jp/pdfdata/JNC-TN7400-99-011.pdf. Accessed 2 Oct 2021

Sibson RH (1984) Roughness at the base of the seismogenic zone: contributing factors. J Geophys Res 89:5791–5799. https://doi.org/10.1029/JB089iB07p05791

Suzuki H, Omura K (1999) Geological and Logging Data of the Deep Observation Wells in the Kanto Region, Japan. Technical Note of the National Research Institute for Earth Science and Disaster Resilience 191. https://doi.org/10.24732/nied.00001805 (**in Japanese with English abstract**)

Tadai O, Lin W, Tanikawa W, Hirose T, Sakaguchi M (2009) Technical note on thermal conductivity measurement for drilled core samples. JAMSTEC Report of Research and Development 9(2):1–14. https://doi.org/10.5918/jamstecr.9.2_1 (**in Japanese with English abstract**)

Takahashi N, Kodaira S, Tsuru T, Park J-O, Kaneda Y, Suyehiro K, Kinoshita H, Abe S, Nishio M, Hino R (2004) Seismic structure and seismogenesis off Sanriku region, northeastern Japan. Geophys J Int 159:129–145. https://doi.org/10.1111/j.1365-246X.2004.02350.x

Takehara M, Horie K, Tani K, Yoshida T, Hokada T, Kiyokawa S (2017) Time-scale of magma chamber processes revealed by U-Pb ages, trace element contents and morphology of zircons from the Ishizuchi caldera, Southwest Japan. Arc Island Arc 26:e12182. https://doi.org/10.1111/iar.12182

Tamanyu S (2008) Classification of wide areas including high-temperature regions from the viewpoint of subsurface temperature distribution—examples of Tohoku and Chugoku/Shikoku districts. Bull Geol Surv Japan 59(1):45–52. https://doi.org/10.9795/bullgsj.59.45 (**in Japanese with English abstract**)

Tamura Y, Tatsumi Y, Zhao D, Kido Y, Shukuno H (2002) Hot fingers in the mantle wedge: new insights into magma genesis in subduction zones. Earth Planet Sci Lett 197:105–116. https://doi.org/10.1016/S0012-821X(02)00465-X

Tanaka A (2009) Lithospheric thermal structure: one of factors influencing depth of earthquakes. Zisin 61(Supplement):S239–S245. https://doi.org/10.4294/zisin.61.239 (**in Japanese with English abstract**)

Tanaka A, Yamano M, Yano Y, Sasada M (2004) Geothermal gradient and heat flow data in and around Japan (I): appraisal of heat flow from geothermal gradient data. Earth Planets Space 56:1191–1194. https://doi.org/10.1186/BF03353339

Tatsumi Y, Furukawa Y, Yamashita S (1994) Thermal and geochemical evolution of the mantle wedge in the northeast Japan arc. 1. Contribution from experimental petrology. J Geophys Res 99(22):275–283. https://doi.org/10.1029/94JB00283

Tatsumi Y, Suenaga N, Yoshioka S, Kaneko K, Matsumoto T (2020) Contrasting volcano spacing along SW Japan arc caused by difference in age of subducting lithosphere. Sci Rep 10:15005. https://doi.org/10.1038/s41598-020-72173-6

Thévenaz L (2006) Review and progress in distributed fiber sensing. Optical Fiber Sensors, Technical Digest (CD) (Optical Society of America, 2006) paper ThC1. https://doi.org/10.1364/OFS.2006.ThC1

Tomiya A (2000) Influence of a magma chamber on thermal structure of the surrounding crust. Bull Volcanol Soc Jpn 45(3):173–179. https://doi.org/10.18940/kazan.45.3_173 (**in Japanese with English abstract**)

Uchida Y, Yoshioka M, Shrestha G (2014) Evaluation of potential for ground-source heat pump system based on hydrological data. BUTSURI-TANSA 67(1):25–36. https://doi.org/10.3124/segj.67.25 (**in Japanese with English abstract**)

Uchida N, Nakajima J, Wang K, Takagi R, Yoshida K, Nakayama T, Hino R, Okada T, Asano Y (2020) Stagnant forearc mantle wedge inferred from mapping of shear-wave anisotropy using S-net seafloor seismometers. Nat Commun 11:5676. https://doi.org/10.1038/s41467-020-19541-y

Uyeda S, Horai K (1964) Terrestrial heat flow in Japan. J Geophys Res 69:2121–2141. https://doi.org/10.1029/JZ069i010p02121

Wada I, Wang K (2009) Common depth of slab-mantle decoupling: reconciling diversity and uniformity of subduction zones. Geochem Geophys Geosyst 10:Q10009. https://doi.org/10.1029/2009GC002570

Wada I, Rychert CA, Wang K (2011) Sharp thermal transition in the forearc mantle wedge as a consequence of nonlinear mantle wedge flow. Geophys Res Lett 38:L13308. https://doi.org/10.1029/2011GL047705

Wessel P, Smith WHF (1998) New, improved version of Generic Mapping Tools released. Eos Trans AGU 79(49):579

Yamano M (1995) Recent heat flow studies in and around Japan, in Terrestrial Heat Flow and Geothermal Energy in Asia. IBH:173–201.

Yamanoi T (2005) Formation of the Yamagata Basin and its circumferential mountains. Quaternary Res Daiyonki-Kenkyu 44(4):247–261. https://doi.org/10.4116/jaqua.44.247 (**in Japanese with English abstract**)

Yano ET, Takeda T, Matsubara M, Shiomi K (2017) Japan unified high-resolution relocated catalog for earthquakes (JUICE): crustal seismicity beneath the Japanese Islands. Tectonophysics 702:19–28. https://doi.org/10.1016/j.tecto.2017.02.017

Yoshida T, Nakajima J, Hasegawa A, Sato H, Nagahashi Y, Kimura J, Tanaka A, Prima ODA, Ohguchi T (2005) Evolution of late Cenozoic magmatism in the NE Honshu Arc and its relation to the crust–mantle structure. Quatern Res 44:195–216. https://doi.org/10.4116/jaqua.44.195 (**in Japanese with English abstract**)

Yoshida T, Kimura J, Yamada R, Acocella V, Sato H, Zhao D, Nakajima J, Hasegawa A, Okada T, Honda S, Ishikawa M, Prima ODA, Kudo T, Shibazaki B, Tanaka A, Imaizumi T (2013) Evolution of late Cenozoic magmatism and the crust–mantle structure in the NE Japan Arc. Geol Soc Lond Special Publ 385:335–387. https://doi.org/10.1144/SP385.15

Yoshida T, Takashima R, Kudo T, Prima ODA, Maeda S, Yoshida K, Okada T, Miura S, Takahashi T, Nagahashi Y, Kataoka K (2020) Late cenozoic igneous activity and crustal structure in the NE Japan Arc: background of inland earthquake activity. J Geogr 129(4):529–563. https://doi.org/10.5026/jgeography.129.529 (**in Japanese with English abstract**)

Yoshioka S, Suminokura Y, Matsumoto T, Nakajima J (2013) Two-dimensional thermal modeling of subduction of the Philippine Sea plate beneath southwest Japan. Tectonophysics 608:1094–1108. https://doi.org/10.1016/j.tecto.2013.07.003

Publisher's Note